# EFFECT OF LOAD PATH ON MODE OF FAILURE AT THE BRITTLE-DUCTILE

# TRANSITION IN WELL-SORTED AGGREGATES OF ST. PETER SAND

A Thesis

by

GOKTURK MEHMET DILCI

Submitted to the Office of Graduate Studies of
Texas A&M University
in partial fulfillment of the requirements for the degree of

MASTER OF SCIENCE

August 2010

Major Subject: Geology

EFFECT OF LOAD PATH ON MODE OF FAILURE AT THE BRITTLE-DUCTILE

TRANSITION IN WELL-SORTED AGGREGATES OF ST. PETER SAND


A Thesis

by

GOKTURK MEHMET DILCI



Submitted to the Office of Graduate Studies of
Texas A&M University
in partial fulfillment of the requirements for the degree of

MASTER OF SCIENCE



Approved by:

| | |
|---|---|
| Chair of Committee, | Frederick M. Chester |
| Committee Members, | Andreas Kronenberg |
| | Walter Ayers |
| Head of Department, | Andreas Kronenberg |


August 2010


Major Subject: Geology

ABSTRACT

Effect of Load Path on Mode of Failure at the Brittle-Ductile Transition

in Well-sorted Aggregates of St. Peter Sand. (August 2010)

Gokturk Mehmet Dilci, B.S., University of Ankara

Chair of Advisory Committee: Dr. Frederick M. Chester

Granular aggregates of quartz subjected to triaxial compression under constant effective pressures ($P_e$) undergo macroscopic failure at critical stress states that depend on the effective mean stress. Although the mode of failure and mechanical response vary systematically with mean stress at failure, prefailure loading at subcritical stress states may induce yielding, and subcritical load paths may influence behavior at failure. Here, I investigate how the failure of quartz aggregates at conditions favoring compaction depends on consolidation history and load path in the transitional and ductile deformation regimes in terms of strain localization and microfracture fabric. Three distinct non-standard triaxial compression load paths were employed; the paths involve different preconsolidation of the aggregates at subcritical isotropic stress followed by differential loading with increasing or decreasing confining pressure. Deformed aggregates were injected with epoxy and studied using optical microscopy techniques to determine microscopic damage evolution for the different load paths. Microfracture data show that preconsolidation at subcritical isotropic loads facilitates formation of campaction bands during subsequent triaxial compression in the transitional regime.

The preferred orientation of intragranular cracks evolves from near random fabrics for isotropic loading to strongly preferred orientations parallel to the maximum principal compression direction for differential loading, with the strongest preferred orientation within the compaction bands. Aside from the preconsolidation, different load paths have only a minor effect on the mechanical response during macroscopic failure.

DEDICATION

To Gulsah, Mom, Dad, Sister, Brother, and Gumus

## ACKNOWLEDGEMENTS

TABLE OF CONTENTS

Page

LIST OF FIGURES

LIST OF TABLES

## 1. INTRODUCTION

Compaction bands are narrow, tabular zones of reduced porosity and permeability that often form during deformation of granular geologic materials [*Mollema and Antonellini,* 1996; *Olsson & Holcomb,* 2000; *Olsson*, 1999]. In nature, compaction bands are oriented perpendicular to the maximum compressive stress. Compaction bands have formed during burial of large grain size (0.3-0.8 mm), granular sediments having high porosity (20-25%) or in the compressional quadrants at the tips of small faults that occur in finer grained (0.05-0.25), and less porous (<20%) sediments [*Mollema and Antonellini,* 1996]. In terms of geometry, compaction bands may be classified as thick (and straight) bands typically 0.5-1.5 cm thick and 5-10 m length, and thin (and crooked) bands typically 0.1-0.5 cm thick and 2 m length [*Mollema and Antonellini,* 1996]. The favorable stress state for compaction band formation is near the brittle-ductile transition, which is at intermediate effective mean stress levels in the vicinity of a transition between dilatant shear failure and compacting cataclastic flow type failure. When the loading paths intersect the failure envelope at much higher mean stresses than the brittle ductile transition, the compactional damage distributes homogeneously rather than concentrating in localized bands.

Compaction bands are characterized by particle size, porosity and permeability reduction, and thus can act as barriers within permeable, granular formations [*Olsson*

---

This thesis follows the style of *Journal of Geophysical Research.*

*& Holcomb* 2000; *Olsson et al.,* 2002]. They can severely compartmentalize subsurface reservoirs and significantly affect the fluid flow characteristics and production feasibility in petroleum and aquifer systems [*Holcomb et al.,* 2007].  If compaction occurs uniformly, it can be beneficial in some cases for the extraction of the pore fluid [*Olsson & Holcomb* 2000]. Accordingly, a better understanding of the mechanics and mechanisms of compaction band formation can improve our ability to predict occurrence of band formation and contribute to developing comprehensive models of fluid flow through reservoir and aquifer systems. Knowledge about compactional behavior of granular materials is also useful for some other applications such as nuclear waste isolation and tunnel settlement [*Jeng et al.,* 2002].

Load path during burial and exhumation history plays a critical role in the mode of failure of natural and laboratory samples of sand aggregates, particularly at the brittle ductile transition. Granular rocks, which had previously undergone an inelastic porosity reduction by exceeding critical stress levels, demonstrate an expanded failure envelope in stress space during subsequent differential loading. This phenomenon is referred to as embrittlement [*Wong et.al.,* 1992]. On the other hand, initial sub-critical triaxial compressive loading at high mean stresses leads the granular materials to yield at lower differential stress levels during successive triaxial compression loadings in the dilatants shear and transition regimes [*Choens and Chester,* 2009].

The purpose of this study is to test the hypothesis that different load paths induce different modes of failure in terms of localization and microfabrics, even if the load

paths intersect at stress states that are equivalent at the macroscopic failure envelope. *Wong et.al,* [1992] and *Choens and Chester* [2009] held the confining pressure values at fixed magnitudes during differential loading. However, for this study, the load paths involve regularly increasing or decreasing confining pressure in harmony with increasing differential stress during the triaxial compression tests, and intersection of the failure envelope at the same stress state. This provides the opportunity to compare evolution of damage for different load paths. I investigated how the distribution of microfractures and the microfracture fabrics change as a reflection of loading path. The load paths employed simulate natural loading during burial and tectonic uplift.

Compaction bands are more readily formed in high porosity granular materials such as loose sands, poorly cemented and well sorted granular rocks or any granular rocks that have coarse or intermediate size grains [*Olsson,* 1999]. For that reason, aggregates of St. Peter sand composed solely of quartz grains were employed for the experiments. The aggregates were comprised of a particle size fraction 250-350 μm diameter. The use of a well sorted, monomineralic aggregate helps avoid significant variations in the starting structure of the samples.

The onset of localization of strain and the initiation of deformation band formation occur as the macroscopic failure strength of a soil or rock is exceeded. At low mean stress conditions, the macroscopic failure strength of granular rocks and loose sands may be described by a Mohr-Coulomb failure relation in which failure strength increases with effective mean stress. At high effective mean stress, failure strength

associated with compactional flow decreases with effective mean stress [*Wong et al.,* 1997; *Baud et al.* 2000]. The stress conditions at failure may be described in terms of the differential stress, Q, and the effective mean stress, P, and illustrated graphically in a Q-P diagram (Figure 1). For high mean stress conditions that favor compactional failure, the failure strength depends strongly on particle size distributions and porosity. The failure relation may be expressed as,

$$Q = (\sigma_1 - P_c) = P^* [\delta \sin \Theta]; \text{ and} \qquad\qquad \text{Eqn. 1}$$

$$P = P^* [\xi + (1-\xi) \cos \Theta] \qquad\qquad \text{Eqn. 2}$$

where P is effective mean stress, $\sigma_1$ is the highest compressive stress, P* is grain crushing pressure, which depends on the strengths of individual grains and grain forming minerals, and $\xi$ and $\delta$ are normalization constants that vary as a function of the particle size distribution in the aggregate. According to this formulation, P* acts as a scaling parameter for the magnitude of the failure stress [*Wong et al.,* 1997]. Accordingly, it can be inferred that the rocks or soils which have different particle size ranges and/or various mineralogical compositions, have different compactional failure strengths. *Karner et al.* [2005a] report that the relations above adequately describe failure strength of St. Peter Sand aggregates determined by triaxial rock deformation experiments (Figure 1).
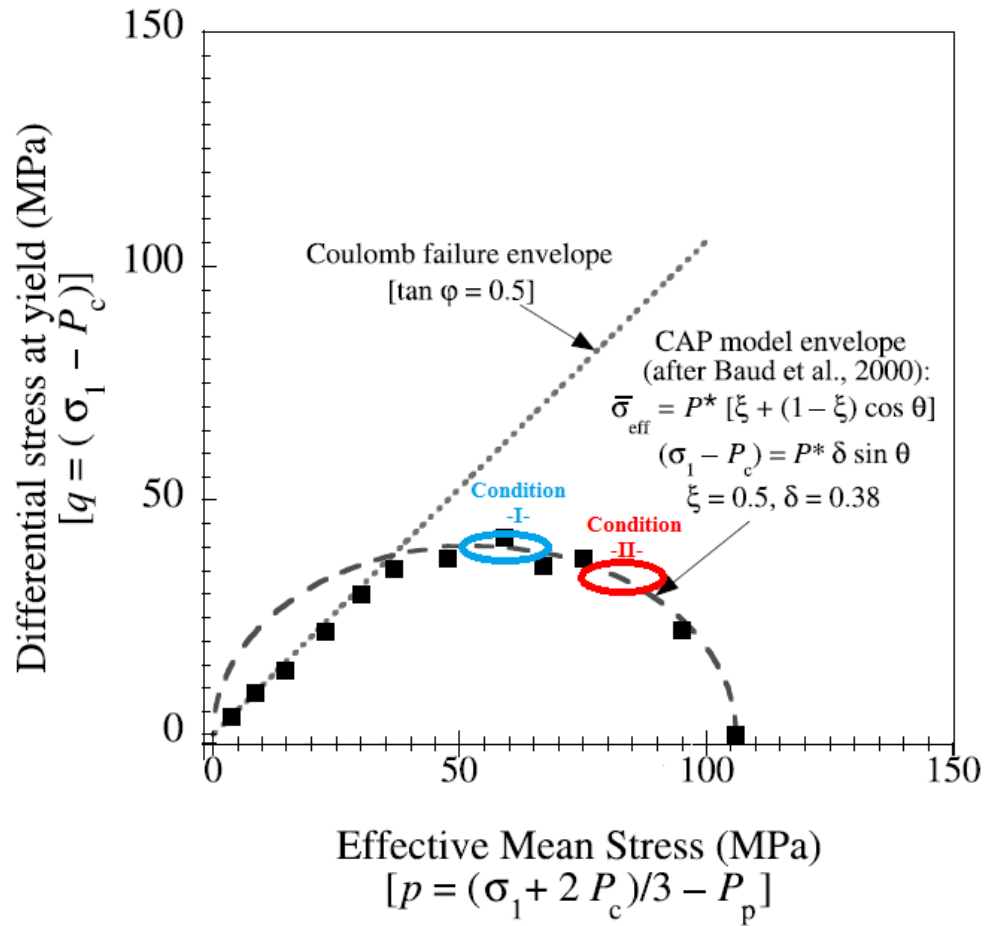
**Figure 1**. Failure conditions investigated in this research. Condition I is the transitional deformation regime, and the Condition II is the ductile deformation regime. The figure was modified from *Karner et al.* [2005a].

## 2.  METHOD

### 2.1.  Experiment Sample and Preparation

Well-sorted, unconsolidated, Ordovician–age St. Peter quartz sand, which was collected from Battle Creek in St. Paul, Minnesota [*Karner et. al.,* 2005a], sieved to achieve a 250-350 μm grain size fraction, was cleaned in an acid bath (5% HCl), washed with distilled water, and air-blown to remove fines (following the procedure of He, 2001). The sand was encapsulated by a cylindrically formed silver foil surrounded by two heat-shrink polyolefin tubes (jackets). Thin Berea sandstone spacers (2.5 mm thick) were placed at the end of the sample in contact with the pore fluid access port to avoid loss of sand grains. During the sample preparation, the sand underwent ultrasonic vibration to produce reproducible initial packing and low starting porosity. The polyolefin jackets were sealed by tie wires along grooves cut in the steel end-cap and piston. The target length and diameter of the cylindrical sand sample were 3.94 cm and 1.9 cm respectively. The mass of sand, and the mass of the sample assembly before and after saturation with water, was measured for each experiment on a digital balance to calculate starting porosity of the samples.  The samples were saturated with distilled water using a vacuum system before insertion into the apparatus for testing [*He,* 2001; *Karner et. al.,* 2003, 2005a].
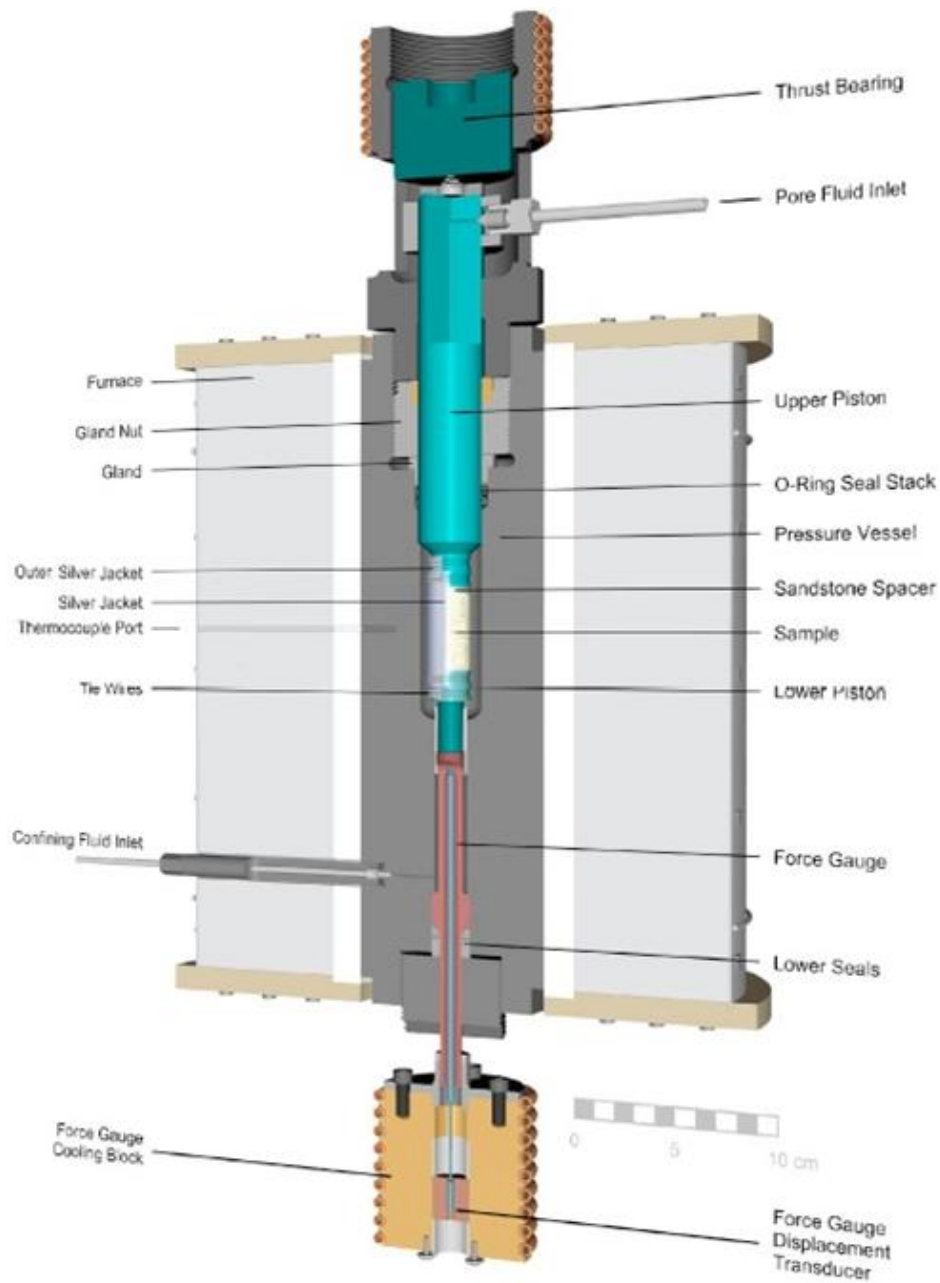
**Figure 2.** Cross sectional rendering of the pressure vessel of the modified variable strain rate (MVSR) triaxial apparatus designed by H. Heard and modified by F. Chester [Heard, 1963; Chester, 1988]. The cross sectional rendering of the vessel is taken from Lenz [2002].

### 2.2. Experiment Procedure

Triaxial compression experiments were conducted on the modified variable strain rate (MVSR) triaxial apparatus in the John Handin Rock Mechanics Laboratory at Texas A&M University to perform hydrostatic and triaxial compression experiments (Figure 2). The MVSR is a liquid confining media, gear driven device ideally suited for testing weak materials.

Ten experiments were conducted to explore the effects of different load paths. The load paths employed different stages and sequencing of isostatic confining pressure, $P_c$, and non-standard triaxial compression loading (Figure 3). In all experiments, we adopt the convention that compressive stresses and compactional strains (i.e., shortening and porosity decrease) are positive, and we denote the maximum and minimum (compressive) principal stresses by $\sigma_1$ and $\sigma_3$, respectively. The pore pressure will be denoted by $P_p$, and the difference between the $P_c$ and $P_p$ will be referred to as the effective pressure, $P_e$. $P_p$ was maintained at 10 MPa (+- 2 MPa) during each test. Each sample was subjected to 12 MPa $P_c$ and 10 MPa $P_p$ at the beginning of each test in order to establish the initial porosity at about 2 MPa effective pressures ($P_e=P_c-P_p=2$ MPa), which is sufficient for the jackets to tightly wrap around the samples. Each experiment involved initial loading to a prescribed $P_e$= 32, 59, 86 and 103 MPa. Subsequently, triaxial compressive loading of the samples was imposed by one of two triaxial load paths following a constant ratio for the change in Q and P. The triaxial compression load paths are characterized by either an increase or decrease in mean stress while increasing

differential stress (Table 1). After completion of triaxial compressive loading, each sample was unloaded, following a reversal of the loading path.

Two suites of experiments were conducted using different $P_e$ and load path sequencing to investigate failure at an intermediate mean stress very near the brittle ductile transition (Q=40 MPa, P=59 MPa), and at higher mean stress, well within the compactional cataclastic flow field (Q=35 MPa, P=80 MPa). $P_e$ sequencing and two triaxial load paths are described in more detail below.
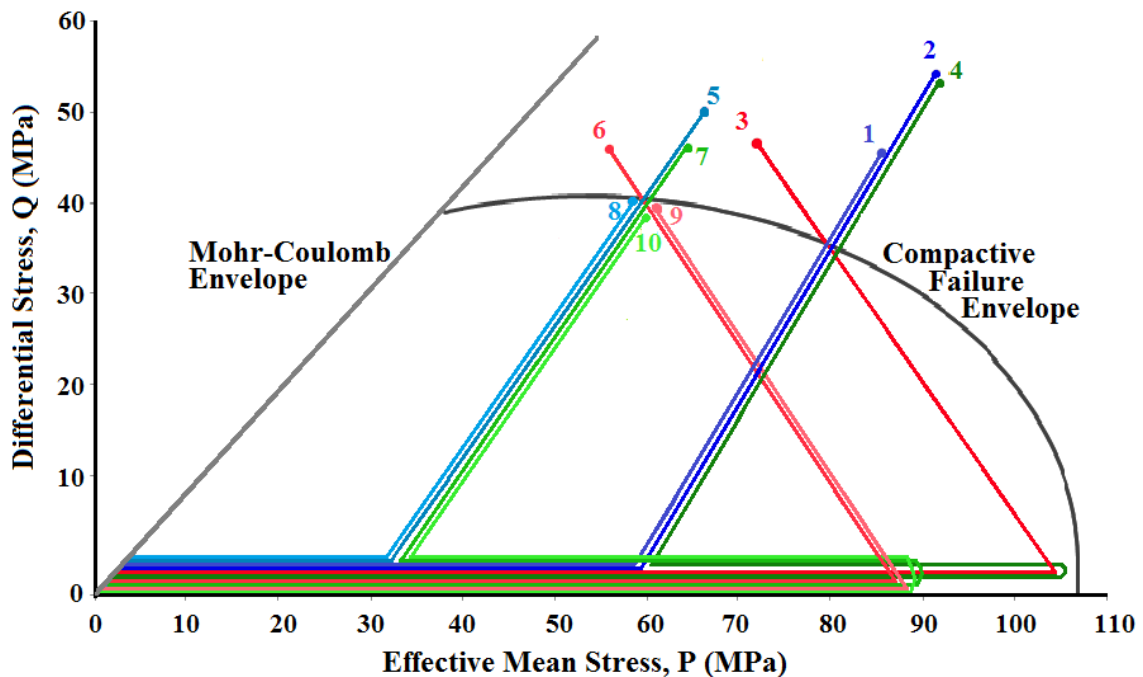


**Figure 3.** The load paths intercepting the compactional failure envelope near the B-D transition field and the ductile field. Load paths with low and intermediate prior isotropic pressurizations and successive triaxial compressions with increasing $P_c$ are shown as blue, the load paths with a high prior isotropic pressurization and successive triaxial compression with decreasing $P_c$ are shown as red, and the load paths that comprise a prior high magnitude isotropic pressurization, a partial isotropic unloading down to the intermediate magnitudes, and differential load starting with those intermediate magnitudes are shown as green.

**Table 1.** Experiment matrix

| Triaxial Compression Load Path | Transitional Regime | Ductile Regime |
|---|---|---|
| Increasing P | Through Yield (Exp. 8)<br><br>Beyond Failure ( Exp 5) | Beyond Failure (Exp. 1, 2) |
| Increasing P after Preconsolidation | Through Yield (Exp. 10)<br><br>Beyond Failure (Exp 7) | Beyond Failure (Exp.4 ) |
| Decreasing P | Through Yield (Exp. 9)<br><br>Beyond Failure (Exp. 6) | Beyond Failure (Exp. 3) |

## 2.3. Triaxial Compression Load Paths

The standard triaxial compression test is at constant $P_e$. In such cases, each incremental increase in the Q corresponds to an increase in the P in the ratio of 1 to 3. However, here we designed load paths that have more dramatic changes in the P values such that the increases in the Q correspond to increases in P in the ratio of 2 to 3 in order to be more similar to the natural burial load path. Also, we designed load paths with decreasing $P_e$ either to create more dramatic initial pressurization difference among load paths or to simulate the load paths of extensional tectonics regions with no sedimentation

or with concurrent erosion. In addition, the load paths with increasing and decreasing $P_e$ were designed to intercept the failure envelope at two target stress states in transitional and ductile regimes.

### 2.3.1. Triaxial Compression Tests with Increasing Confining Pressure

The triaxial compression load paths characterized by increasing P with increasing Q according to

$$d\,(Q) = 3/2\,d\,(P) \hspace{4cm} \text{eqn 3.}$$

were achieved by continuously varying Pc with Q and $\sigma_1$ according to

$$d\,(Q) = 3*d\,(P_c) \hspace{4cm} \text{eqn 4.}$$

$$d\,(\sigma_1) = 4*d\,(P_c) \hspace{4cm} \text{eqn 5.}$$

This ratio is quite close to the ratio of vertical and horizontal load increases over natural burial which is reckoned as

$$d\,(\sigma_v) \approx 3*d\,(\sigma_h) \hspace{4cm} \text{eqn 6.}$$

An analogous load path may be encountered in nature within extensional tectonics regions with overburden load increasing by sedimentation in rift valleys or graben basins, such that horizontal extensional stresses reduce the horizontal stresses which occur depending on Poisson ratio. The suites of experiments having this particular triaxial compression load path are shown in Q-P space in figure 3.

### 2.3.2. Triaxial Compression Tests with Decreasing Confining Pressure

The triaxial compression load paths characterized by decreasing P with increasing Q according to

$$d(Q) = -3/2\ d(P) \qquad\qquad\qquad \text{eqn 7.}$$

were achieved by continuously varying Pc with Q and σ1 according to

$$d(Q) = -\ d(P_c)\ \text{and} \qquad\qquad\qquad \text{eqn 8.}$$

$$d(\sigma_1) = 0;\ \text{and}\ d(P_c) < 0 \qquad\qquad\qquad \text{eqn 9.}$$

An analogous load path may be encountered in nature within extensional tectonics regions with no increase in overburden by sedimentation or with concurrent erosion. Such stress states can form by extension of strata overlying rising plutonic domes or salt diapers.

The suites of experiments with this particular triaxial compression load path are shown in Q-P space in figure 3.

### 2.3.3. Load Path Sequencing

Three isostatic differential pressure load paths were used prior to implementing the triaxial compression stage as shown in figure 3.

A. For the samples that underwent the triaxial load paths with decreasing P (eqn 7), the samples were first loaded to high $P_e$ magnitudes of 103.3 MPa and 86 MPa such

that subsequent triaxial load paths would intersect the failure envelope at the two target values.

B. For samples that underwent the triaxial load paths with increasing P (eqn 3), the samples were first loaded to lower $P_e$ magnitudes of 59 MPa and 32 MPa, such that subsequent triaxial load paths would intersect the failure envelope at the two target values.

C. An additional isostatic pressurization sequence was employed for the samples that underwent the triaxial load paths with increasing P (eqn 3). In this case the isostatic loading began with pressurization to 103.3 MPa and 86 MPa as described in section A above, and then held at those effective pressures for 3.5 hours. Subsequently, the effective pressures were reduced to the magnitudes that were achieved in pressurization sequence B above, i.e., isostatic effective pressure levels of 59 MPa and 32 MPa. After these pressures were achieved, triaxial loading was imposed

## 2.4. Mechanical Data Analysis

Applied differential axial force (F), confining and pore fluid pressures ($P_c$, $P_p$), pore volume change (dV), axial displacement (d), and elapsed time (t) data were collected by an internal force gauge, volumometers, displacement transducer and system timer during the experiments. The raw mechanical data were used to calculate differential stress (Q), effective mean stress (P), volumetric strain ($\beta$) and axial strain ($\epsilon$) during and after the experiments. Measurement accuracies are ±0.3 MPa for Q and P, ±0.5 MPa for $P_c$, ±0.025 MPa for $P_p$, ±0.03 % for $\beta$ and ±0.02 % for $\epsilon$ [based on personal

conversation with *F.M. Chester]*. Data recording increment was set at 1 Hertz. The desired load paths were achieved by maintaining $P_p$ constant and by simultaneously adjusting the confining pressure to target levels calculated in real time by the computer according to relations presented above (eqn 3, 4, 5, 7, 8, and 9). Initial and post experiment pore volumes of specimens were determined making mass measurements for dry-undeformed, saturated-undeformed, and saturated-compacted-deformed states of the specimens. For each sample, the final porosity, $\Phi_f$, was determined by mass measurements, and used as a reference together with the dV ($cm^3$) data collected from the volumometers to determine porosity values for the starting condition of each experiments, $\Phi_o$, at the time of differential loading, $\Phi_L$, at the peak differential load, $\Phi_{Qmax}$, and when differential unload was removed, $\Phi_u$ (Table 2). We also adopted the slope of the Q vs. ε curves as "apparent stiffness" (E'). Because of abnormal permanent axial strain that occurred during early stages of the differential loading stages of some experiments, I calculated E' values from the slope of differential unloading curves (Table 2). The second derivative of the stress (P and Q) versus strain (ε and β) curve was used as an objective approach to determine yield and failure strengths for all experiments.

To determine the accumulation of permanent (plastic) volume strain during loading, the elastic volumetric strain was subtracted from the total volume strain. Elastic volume strain is determined from the unloading portion of each test at the end of each experiment. There is little permanent strain accumulation during unloading. The elastic volume strain vs. mean stress during unloading for all tests can be fit by a master curve (Figure 4).

**Table 2.** Experiment summary

| Exp # | $\Phi_o$ (%) | $\Phi_L$ | $\Phi_{Qmax}$ | $\Phi_u$ | $\Phi_f$ (%) | E' (MPa) | $Q_{yield}$ (MPa) | $Q_{failure}$ (MPa) | $Q_{max}$ (MPa) | $P_{yield}$ (Mpa) | $P_{failure}$ (Mpa) | $P_{Q.max}$ (Mpa) | $Pe_o$ (Mpa) | $Pe_{max}$ (Mpa) |
|---|---|---|---|---|---|---|---|---|---|---|---|---|---|---|
| S-01 | 34 | 31.5 | 30.4 | 30.9 | 33.2 | 56.7 | 35.14 | 40.50 | 44 | 78 | 82 | 86 | 59 | 59 |
| S-02 | 32.5 | 30 | 28 | 28.4 | 30.5 | 57.1 | 51 | 54.09 | 54 | 82.5 | 86 | 92.3 | 59 | 59 |
| S-03 | 35.9 | 32.2 | 32.4 | 31.8 | 34.5 | 130 | 33 | 45.28 | 47 | 81.5 | 75.5 | 73 | 103.3 | 103.3 |
| S-04 | 34.3 | 31.2 | 30.2 | 30.7 | 32.6 | 54 | 42.5 | 49 | 52 | 82 | 87 | 91.7 | 59 | 103.3 |
| S-05 | 33.8 | 31.4 | 31.2 | 31.7 | 33.3 | 55 | 34.44 | 37.84 | 48.6 | 61 | 65 | 64.7 | 32 | 32 |
| S-06 | 35 | 32.1 | 31.9 | 31.1 | 33.6 | 106 | 44.9 | 45.18 | 45 | ? | 56.5 | 56.6 | 86 | 86 |
| S-07 | 37.2 | 35.2 | 34 | 34.4 | 35.9 | 52.5 | 42 | 44.57 | 45 | 59.5 | 62.5 | 62 | 32 | 86 |
| S-08 | 34 | 32.6 | 31.4 | 31.9 | 33.4 | 37.5 | 37.04 | 38.92 | 39 | 54.5 | 58 | 57.1 | 32 | 32 |
| S-09 | 33.5 | 30.3 | 30.7 | 30.3 | 32.6 | 157 | 37.53 | - | 40 | 65 | ? | 59.6 | 86 | 86 |
| S-10 | 35.4 | 33.1 | 32.3 | 32.8 | 34.3 | 50.3 | 30.18 | - | 39.3 | 56 | ? | 58 | 32 | 86 |
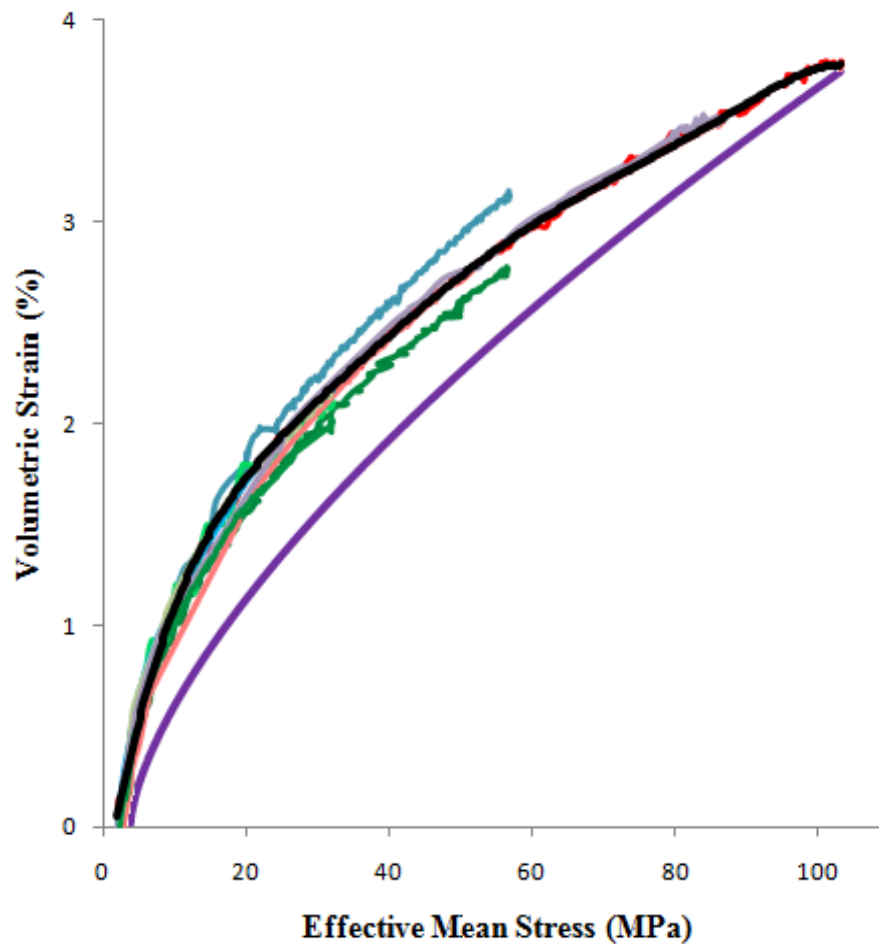
**Figure 4.** Observations and models of poroelastic behavior of sand aggregates in a volumetric strain versus effective mean stress plot. The unloading curves from several different experiments are shown. The black curve is the best fit using a simple polynomial equation. The best fit polynomial is used as master elastic curve to determine plastic volume strain from the experiments (see text). The purple curve shows the fit using the result of theoretical model of a porous granular aggregate of simple spheres and Hertzian-type contacts [*Karner et al., 2003*] This relation was not employed as it did not fit the observations adequately.

**2.5.    Post-Experiment Sample Preparation**

The compacted, saturated samples were weighted after unloading at the end of the experiments to determine mass of water in the samples, and thus determine the volume of pore space in the deformed samples. The final porosities were determined from total volume calculations including sand volumes determined from sand mass measurements and density of quartz. I combined the volume change data gathered from the volumometers during tests with the final porosity values that I take as a reference to determine the evolution of porosity changes (and thus volumetric strain) from the end of the experiments to the starting conditions.

After each experiment, the sample was dried in a laboratory oven and saturated with blue-dyed epoxy. Epoxy filled samples were cut in half parallel to the cylinder axis using a precision low speed diamond saw to avoid generating new cracks, and to prepare doubly polished petrographic sections. Cut surfaces were prepared by sequential grinding with 400-600-1000 grit silicon carbide powders, and then polishing with 3 and 0.3 micron alumina powders. Thin sections (10-20 µm thickness) were studied using optical techniques to characterize microstructure.

**2.6.    Microscopic Studies**

Petrographic sections of samples were analyzed using optical microscopy to determine the orientation distribution and the spatial density distribution of microfractures. Orientations of 77 and more (112 the most) intragranular cracks

throughout the thin sections were measured on a flat microscope stage and analyzed

assuming axial symmetry.
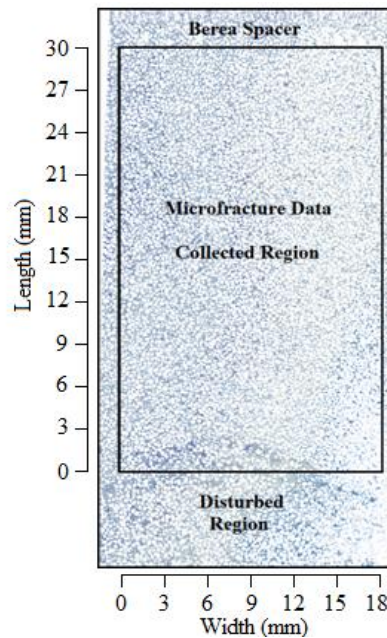


**Figure 5.** Preferred orientation, density distribution and linear crack density data were collected within the indicated region of the thin sections.

The density distribution of cracks within samples was determined following the

method of *Menendez et al.* [1996]. Using the thin sections and thin section photographs,

I established orthogonal gridded scan lines spaced 3 mm over the undisturbed part of the

samples (Figure 5). The grid lines are perpendicular and parallel to the shortening

direction. The linear crack density, defined as the number of crack intercepts per unit

length was determined on each 3mm scan line segment. Linear crack densities along

scan lines that are perpendicular and parallel to the shortening direction were denoted as

$L_1$ and $L_2$ respectively.

I also measured the quantity and angular orientation of cracks within whole samples, in concentrated deformation regions, and in host domains to determine preferred orientation of the cracks.

## 3.  RESULTS

### 3.1.  Microstructure

Consolidation of the sand samples appears homogeneous at the macroscopic scale, but petrographic observations indicate many grains are fractured and displaced at the microscopic scale throughout the sample. Samples deformed in the transitional field have localized zones of concentrated deformation, whereas samples deformed in the ductile field exhibit distributed, homogeneous deformation. Accordingly, the microscopic deformation characteristics are quantified for all the samples deformed in the transitional field with either increasing P or decreasing P load paths.

### 3.1.1.  Microfracture Density Distribution

The density distribution of microfractures, as illustrated by local mean densities, $P_L$, of the counted cracks, are shown in contour maps of the six specimens deformed in the transitional regime. Distinct zones of localized compaction indicated by high microfracture density are evident in samples deformed beyond failure under increasing P after preconsolidation (#7) and under decreasing P (#6) (Figure 6). Some evidence of incipient localization of compaction is apparent in samples deformed through yield (#8) and beyond failure (#5) under increasing P. On the other hand, compactional damage is distributed in samples deformed through yield under increasing P after preconsolidation (#10) and under decreasing P (#9). The local mean densities of the cracks counted on the 3 mm scan lines are increased in the lower quarters of the samples deformed beyond failure under decreasing P (#6), or increasing P after preconsolidation (#7). At the scale

of the 3 mm grid maps, zones of concentrated deformation appear as parallel elongate in directions at high angle to load axis (Figure 7).
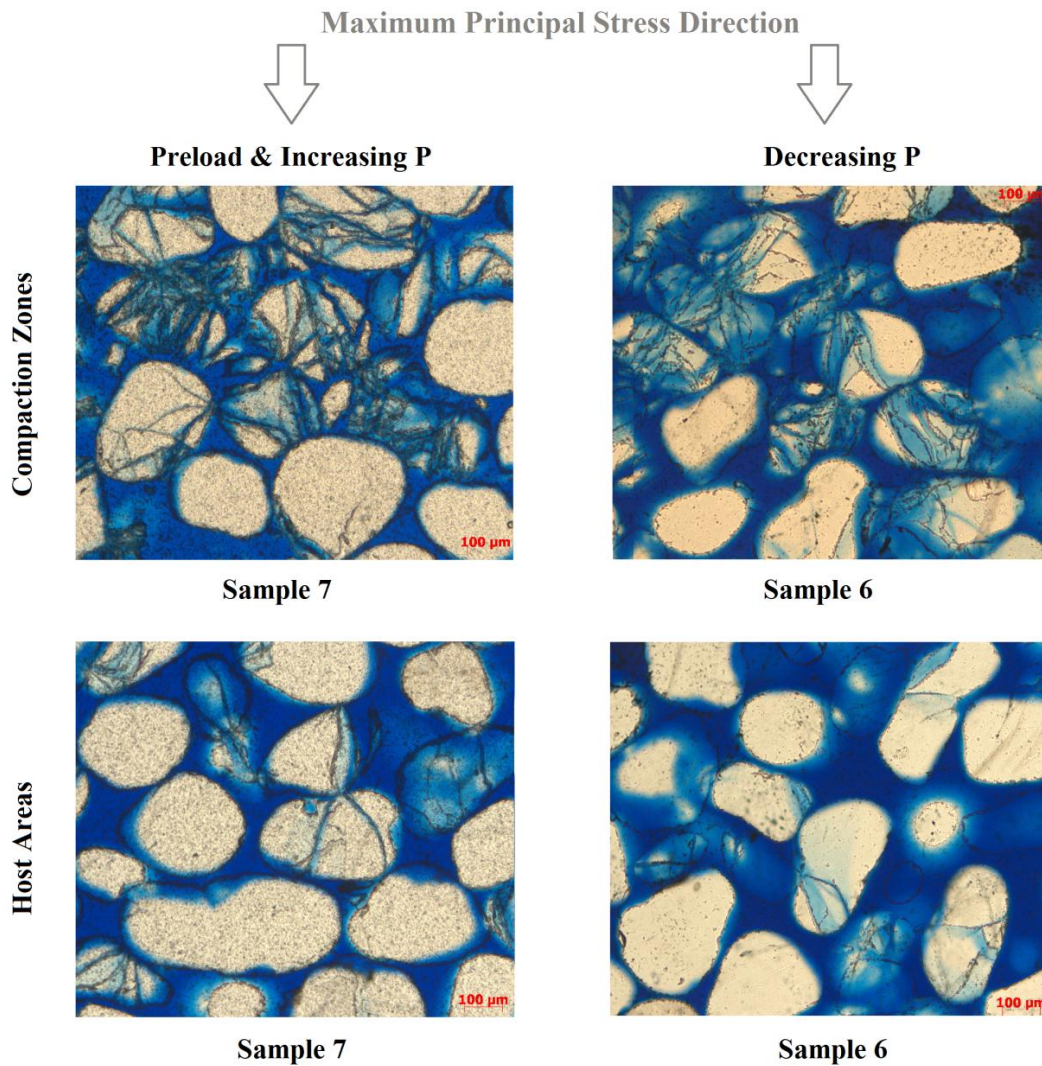


**Figure 6.** Photomicrographs of the representative parts of samples deformed with increasing P with an initial high magnitude isotropic pressurization (#7) and under decreasing P (#6). The samples #6 and #7 best developed localized compactional deformation zones.
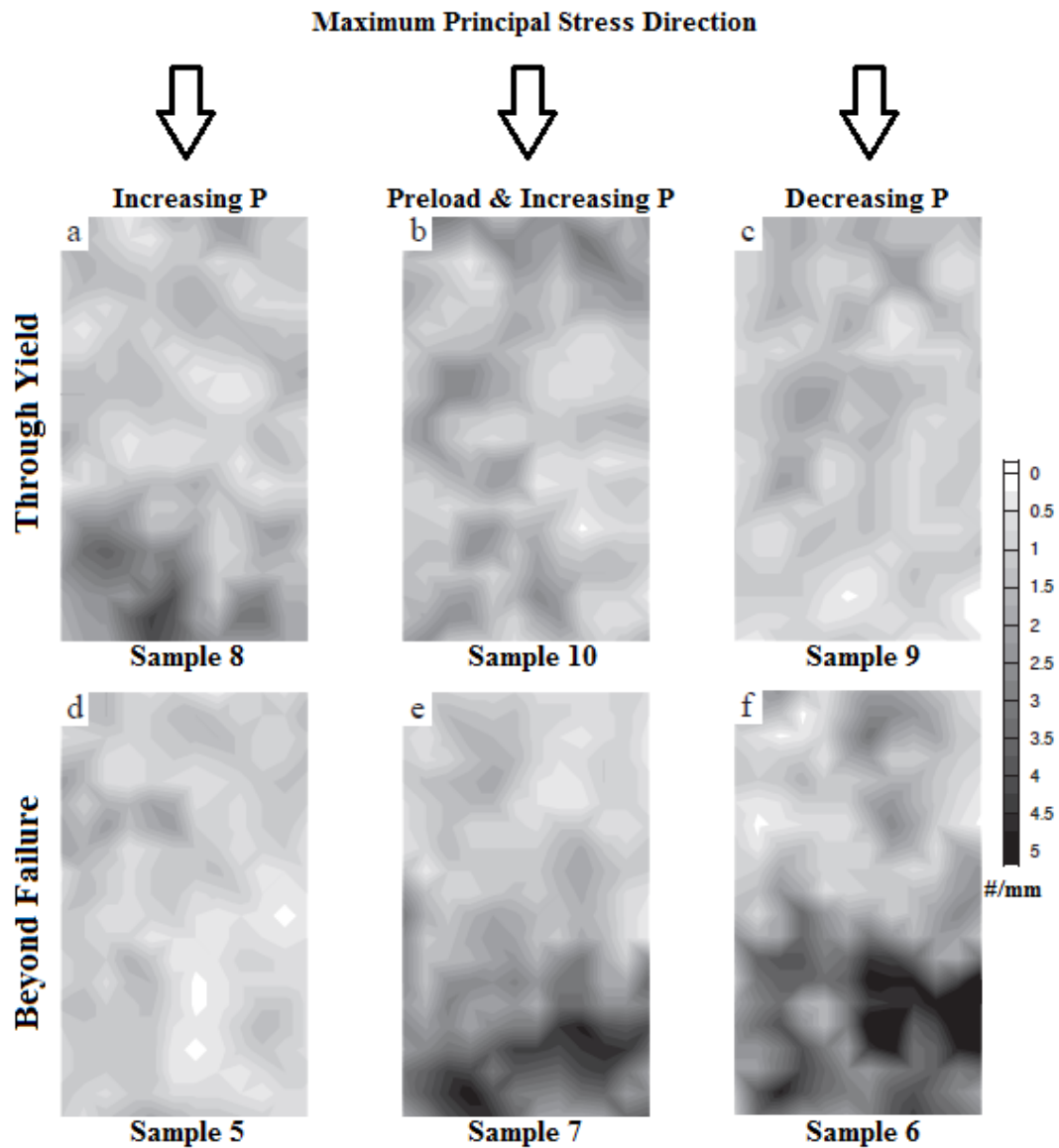
**Figure 7.** Shaded contour maps of the distribution of microfracture damage in six of the deformed specimens. The linear fracture (#/mm) density is contoured in maps of the petrographic sections cut through the center of the samples parallel to the cylinder axis. Borders of mapped region shown in Figure 5.

Microfracture densities in samples are generally greater in samples deformed beyond failure than those loaded only through yield. For samples containing compactional deformation bands, the average $P_L$ inside the band is generally about twice that in the surrounding host aggregates in all samples, the average linear fracture density determined from traverses perpendicular to the load axis, $L_1$, and parallel to the load axis, $L_2$, are similar  (Table 3). $L_1/L_2$ ratios range between 0.88 and 1.4, consistent with an anisotropic fracture orientation distribution. The $L_1/L_2$ ratios in compactional deformation bands are generally greater than in the neighbor host aggregate, suggesting greater fracture anisotropy inside bands (Table 3).

The greatest increase in the $L_1/L_2$ ratios from the neighboring aggregates to within the compactional bands appear in the sample deformed to beyond failure under increasing P after preconsolidation (#7). In contrast, the increase in $L_1/L_2$ ratio from host aggregate to the compactional band is least for the specimen deformed under increasing P without preconsolidation.

**Table 3.** Microfracture density of samples deformed in the transitional regime.

| Exp. # | Portion of Sample | $L_1$* #/mm$^{-1}$ | $L_2$* #/mm$^{-1}$ | $L_1/L_2$ | $P_L$ #/mm$^{-1}$ | $\beta$ (%) |
|---|---|---|---|---|---|---|
| 5 | Host Aggregate | 0.803 | 0.888 | 1.107 | 0.845 | - |
| 5 | Compactional Zone | 1.185 | 1.063 | 1.114 | 1.124 | - |
| 5 | Whole specimen | 0.969 | 0.881 | 1.100 | 0.925 | 0.85 |
| 6 | Host Aggregate | 1.617 | 1.91 | 0.846 | 1.763 | - |
| 6 | Compactional Zone | 3.805 | 3.857 | 0.986 | 3.831 | - |
| 6 | Whole specimen | 2.015 | 2.300 | 0.876 | 2.157 | 2.09 |
| 7 | Host Aggregate | 1.622 | 1.589 | 1.020 | 1.605 | - |
| 7 | Compactional Zone | 3.888 | 3.095 | 1.256 | 3.491 | - |
| 7 | Whole specimen | 1.828 | 1.890 | 0.967 | 1.859 | 2.02 |
| 8 | Host Aggregate | 1.259 | 1.270 | 0.991 | 1.264 | - |
| 8 | Compactional Zone | 2.528 | 2.214 | 1.142 | 2.371 | - |
| 8 | Whole specimen | 1.489 | 1.404 | 1.061 | 1.446 | 0.97 |
| 9 | Whole specimen | 1.065 | 1.052 | 1.013 | 1.058 | 1.31 |
| 10 | Whole specimen | 1.626 | 1.157 | 1.405 | 1.391 | 1.81 |
| LSP01 | Whole specimen | - | - | - | 1.870 | 2.13 |
| LSP03 | Whole specimen | - | - | - | 0.590 | 1.05 |

* $L_1$ and $L_2$ is linear fracture density in traverses perpendicular and parallel to load axis, respectively

On the other hand, the preferred orientations of the cracks within the zones of relatively higher $P_L$ are sub-parallel to the load axis in the samples deformed beyond failure under increasing P after preconsolidation (#7) and under decreasing P (#6) (Figures 8 and 9).
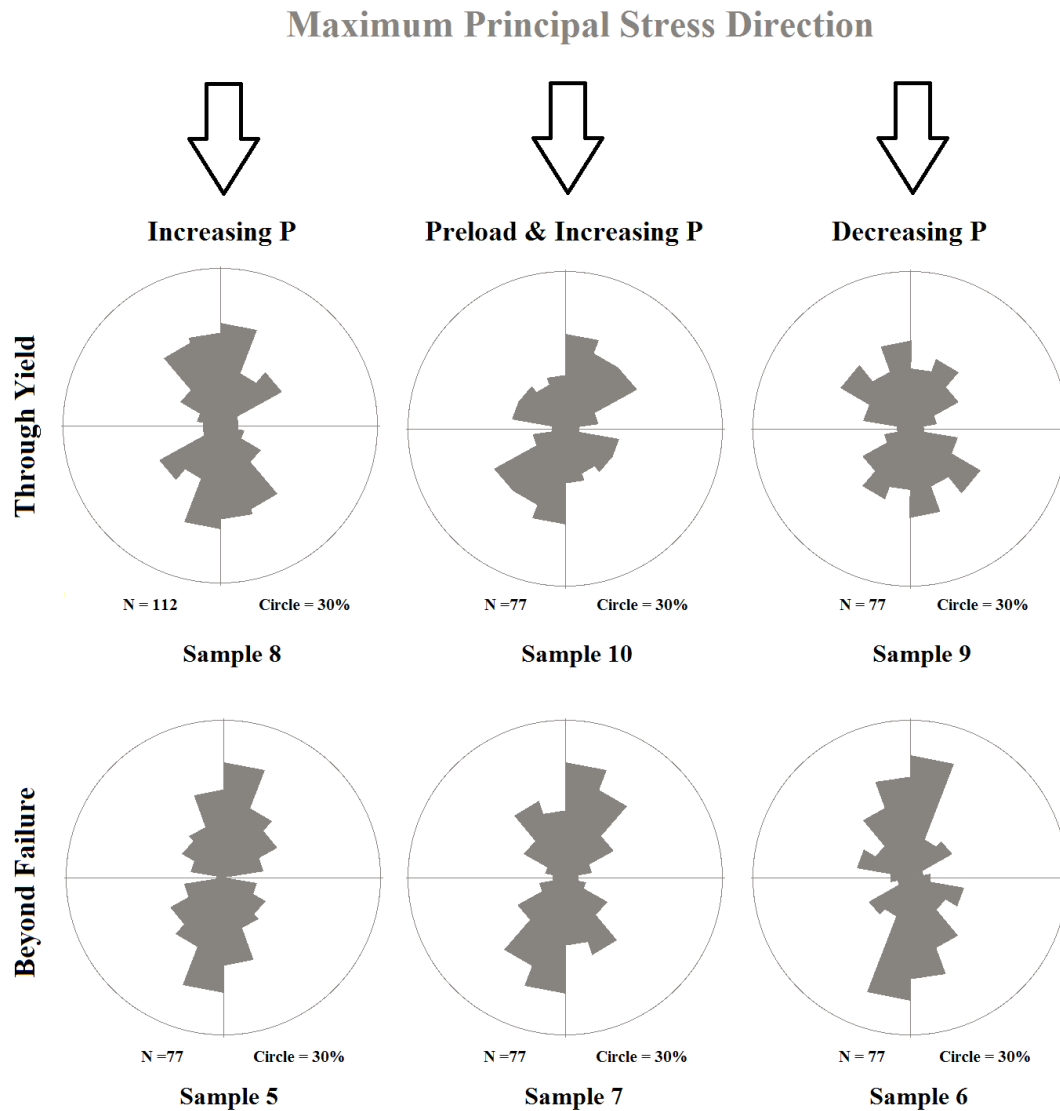
**Figure 8**. Preferred orientation of microfractures in samples deformed in the transitional regime as a function of load path and magnitude of deformation. Orientations determined from petrographic sections cut through center of the specimen and parallel to the maximum principal compressive axis. Outer perimeters of the rose diagram are the same frequency, 30%, in all diagrams. Number of measurements is indicated.
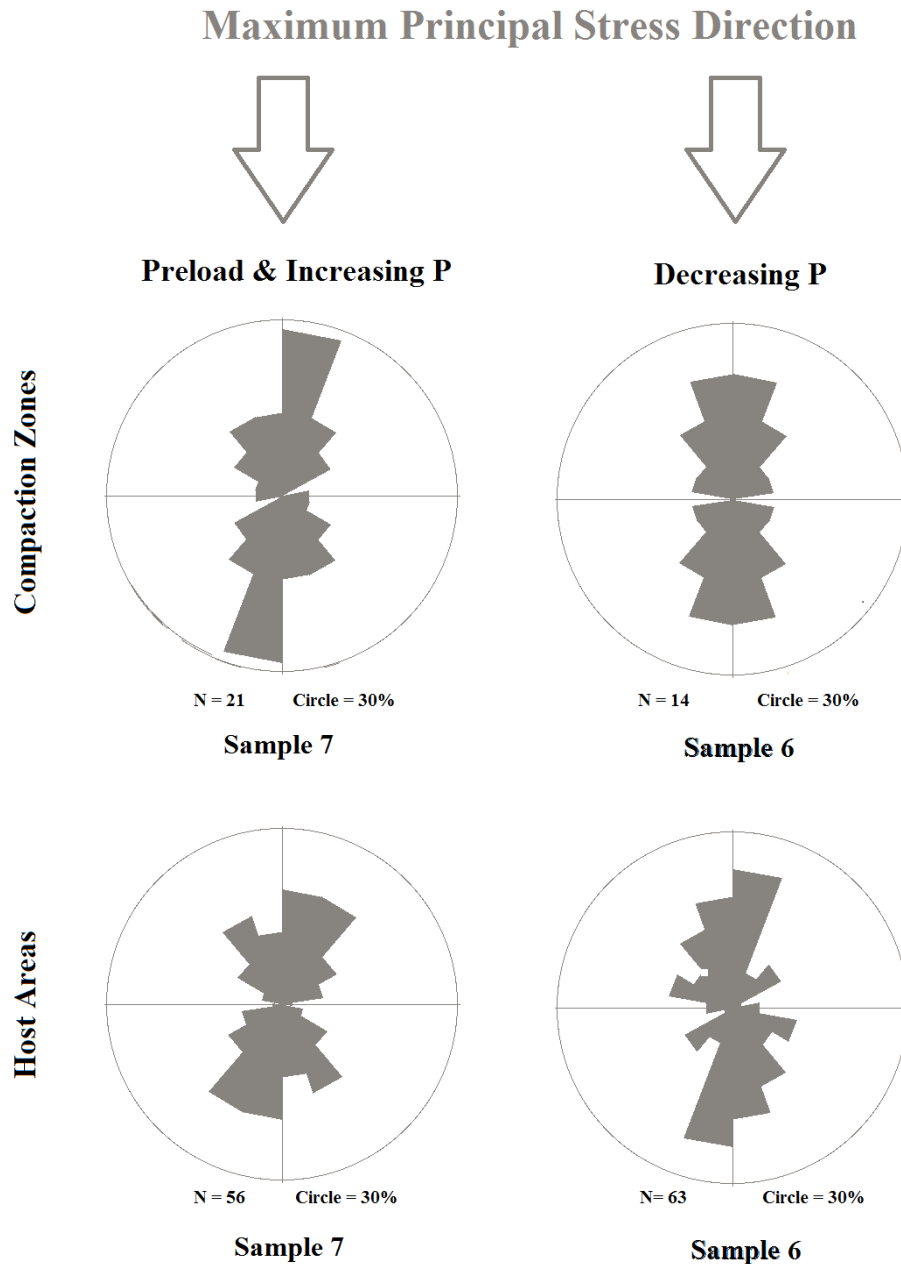
**Figure 9.** Preferred orientation of microfractures in the compactional deformation zones and in surrounding host aggregate of the samples, which show evident localization, deformed in the transitional regime as a function of load path and magnitude of deformation. Orientations determined from petrographic sections cut through center of the specimen and parallel to the maximum principal compressive axis. Outer perimeters of the rose diagram are the same frequency, 30%, in all diagrams. Number of measurements is indicated.

### 3.1.2. Microfracture Orientation Distribution

The microfracture fabric of the sample deformed in the transitional regime generally shows a preferred orientation of microfracture, with cracks aligned parallel to the maximum compressive stress direction. Samples deformed through yield show the lowest preferred orientations, where the sample deformed under decreasing P (#9) displays the microfracture fabrics. The sample deformed under increasing P (#8) displays the strongest preferred orientation among the three samples deformed to failure in the transitional regime with different load paths. Samples deformed beyond failure, the load path of increasing P (#5) leads to the strongest preferred orientation of microcracks parallel to the maximum compressive axis. However, the other two load paths display similar, anisotropic fabrics as well.

In general, the strongest microfracture anisotropy is seen in the localized compactional zones. The preferred orientations of the microfractures within localized compactional zones are most obvious for the samples loaded with increasing P after preconsolidation (#7) and with decreasing P (#6). The preferred orientation of the microfractures is almost perfectly parallel to the maximum principal stress axis.

### 3.2. Mechanical Results

### 3.2.1. Ductile Regime

The mechanical response of samples deformed in the ductile regime is similar to each other overall, but there are important differences in behavior for the different load

paths incorporating preconsolidation and either increasing or decreasing P during differential loading.  In the granular aggregates tested, significant elastic and plastic strain develops during the isostatic stressing as the effective confining pressure is increased prior to differential loading.  During the increase in effective pressure, total volumetric strains of approximately 3.5 to 5% are achieved (Figure 10). Including the isostatic and differential loading portion of the tests, total volumetric strains of 5 and 6% are achieved.
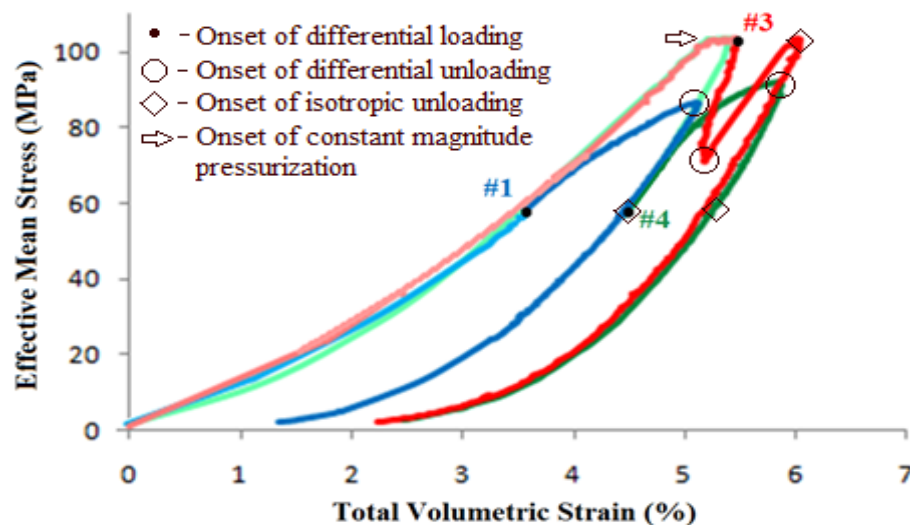


**Figure 10.** Effective mean stress, P, versus total (elastic & plastic) volumetric strain for samples loaded beyond failure in the ductile regime. Load paths shown are increasing mean stress (#1, blue curve), increasing mean stress after preconsolidation (#4, green curve), and decreasing mean stress (#3, red curve). Black dots show the initiation of differential loading.

As expected for porous granular aggregates under isostatic stressing, the P versus total volumetric strain curves display concave upward shapes for both loading and unloading paths (Figure 10). The similar shapes of curves for loading and unloading suggest strain is dominantly, though not necessarily completely, poroelastic during these

stages of the tests.  Under differential loading the curves display concave downward

shapes in plots of Q versus total axial strain, consistent with an increase in plastic strain

with increase in Q (Figure 11).
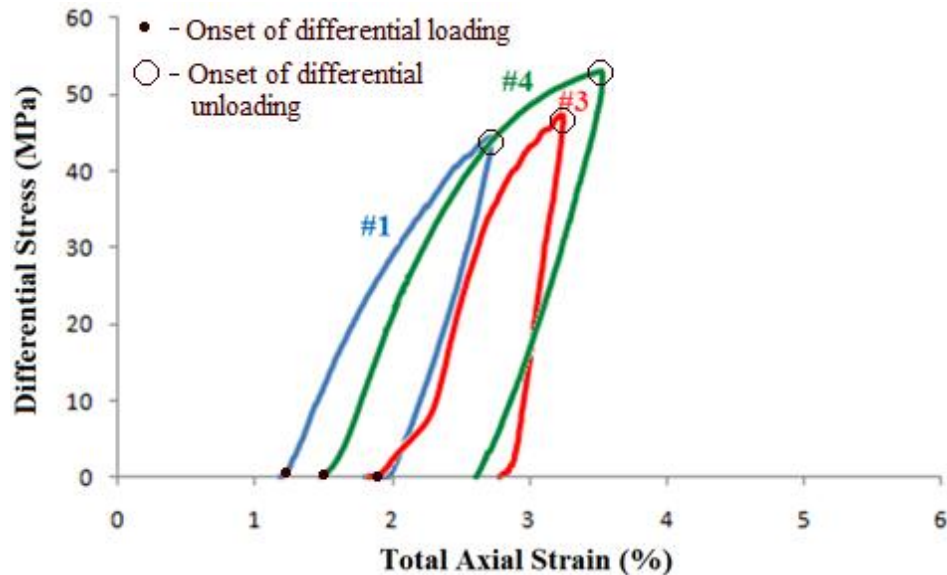


**Figure 11.** Differential stress, Q, versus total axial strain for samples loaded beyond failure in the ductile regime. Load paths shown are increasing mean stress (#1, blue curve), increasing mean stress after preconsolidation (#4, green curve), and decreasing mean stress (#3, red curve).

Although the total volume strain and total axial strain at the onset of differential

loading differ for the three load paths, the change in the axial strain for differential

loading through yield is similar, approximately 1% axial strain, for all three (#1, #3 and

#4) load paths (Table 4).  However, the volume strains during differential loading vary

dramatically, from 0.9% for the increasing P (#1) load path, and -0.2% for the

decreasing P (#3) load path (Table 4).  Furthermore, the partitioning between elastic and

plastic strain is different for the three load paths. Additional detail in the accumulation

and partitioning of elastic and plastic strain can be obtained from the plots of P and Q

versus plastic volume strain (Figure 12).

**Table 4.** Strain differences from the beginning of differential loads to the failure stress (C*) for the samples deformed in the ductile regime.

| Triaxial Compression Load Path | $\Delta\beta$ (%) | $\Delta\beta_p$ (%) | $\Delta\beta_e$ (%) | $\Delta\varepsilon$ (%) |
|---|---|---|---|---|
| Increasing P (#1) | +0.9 | +0.5 | +0.4 | +1.05 |
| Increasing P after Preconsolidation (#4) | +0.6 | +0.25 | +0.35 | +0.90 |
| Decreasing P (#3) | -0.2 | +0.15 | -0.35 | +0.95 |
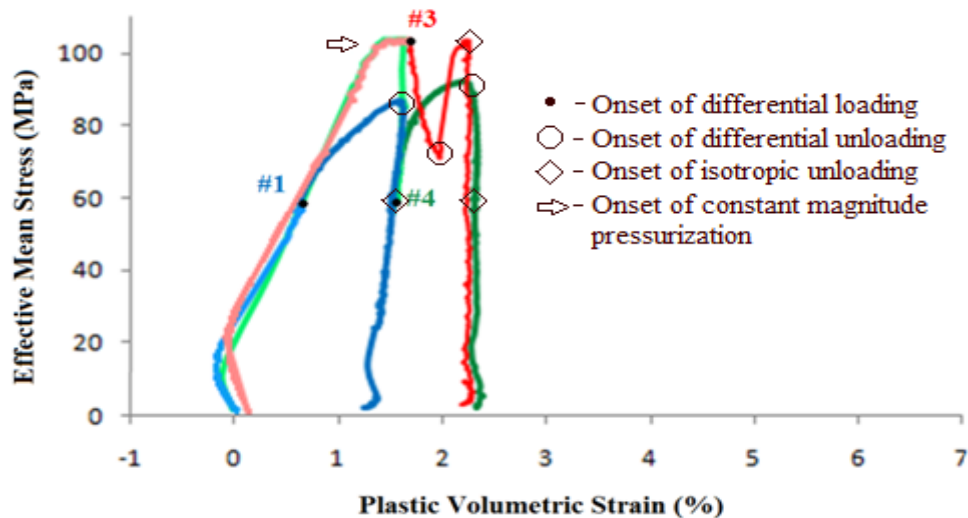


**Figure 12**. Effective mean stress, P, versus plastic volumetric strain for samples loaded beyond failure in the ductile regime. Load paths shown are increasing mean stress (#1, blue curve), increasing mean stress after preconsolidation (#4, green curve), and decreasing mean stress (#3, red curve).

In the ductile regime, significant plastic strain accumulates during the initial

isotropic loading at P greater than approximately 55 MPa and during creep under high-

magnitude isostatic stress in the preconsolidation portion of the increasing P test (#4)

and before initiating differential loading in the decreasing P tests (#3) (Figure 12).

Plastic strain also occurs during differential loading regardless of load path, where

significant plastic strain begins to accumulate at differential stress of approximately 30

MPa (Figure 13). For both increasing P load paths (#1, and #4), regardless of whether a

preconsolidation stage is employed, plastic strain accumulates only during increasing Q.

In contrast, for the decreasing P load path (#3), plastic strain accumulates during both

increasing and decreasing Q (Figure 13).  The behaviors reflect the dependence of

compactional strain on both P and Q in the ductile regime.
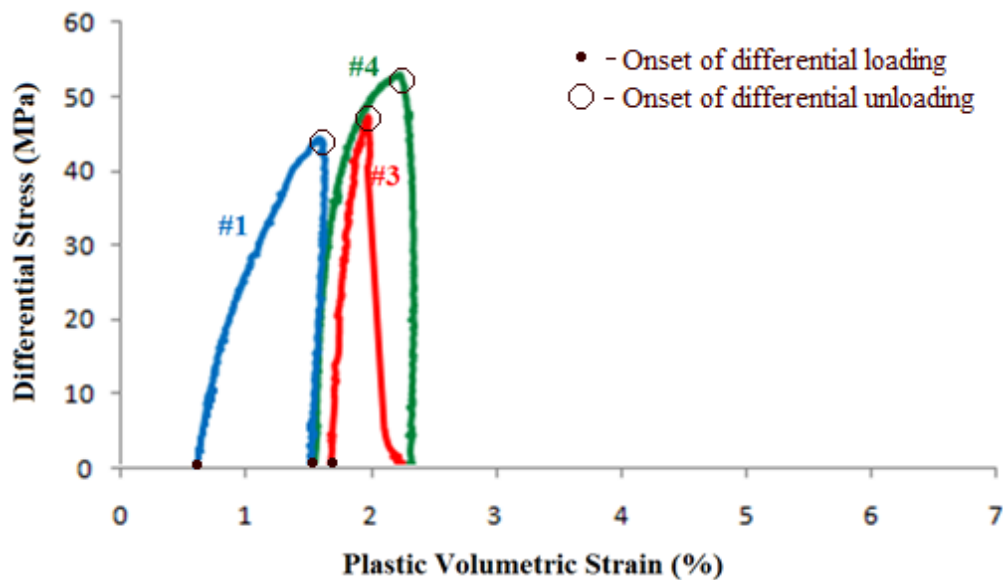


**Figure 13.** Differential stress, Q, versus plastic volumetric strain for samples loaded beyond failure in the ductile regime. Load paths shown are increasing mean stress (#1, blue curve), increasing mean stress after preconsolidation (#4, green curve), and decreasing mean stress (#3, red curve).

All the samples deformed in ductile regime exhibit strain hardening after failure; however the slopes of the stress-strain curves show that the sample deformed under a decreasing P load path (#3) showed the greatest hardening after the failure, and the greatest apparent stiffness during the differential loading stage, relative to the other two samples deformed under increase P load paths (Figure 11).

### 3.2.2. Transitional Regime

Although samples were deformed to two stages (i.e., through yield and beyond failure), the mechanical behavior is reproducible and therefore only the mechanical results of tests taken beyond failure are presented (Exp 5, 6, and 8).

The mechanical response of samples deformed in the transitional regime is similar overall, but there are some important differences in behavior for the different load paths. As was seen in the experiments in the ductile regime, significant elastic and plastic strain develops during the isostatic stressing as the effective confining pressure is increased prior to differential loading. During the increase in effective pressure, total volumetric strains of approximately 1.8 to 4.2% are achieved prior to differential loading (Figure 14). Total volumetric strains between 4 and 6% are achieved including the isostatic and differential loading portion of the tests,. The total volumetric strains are similar to those achieved in the ductile regime experiments due to the contribution of post failure compaction localization in the transitional regime.
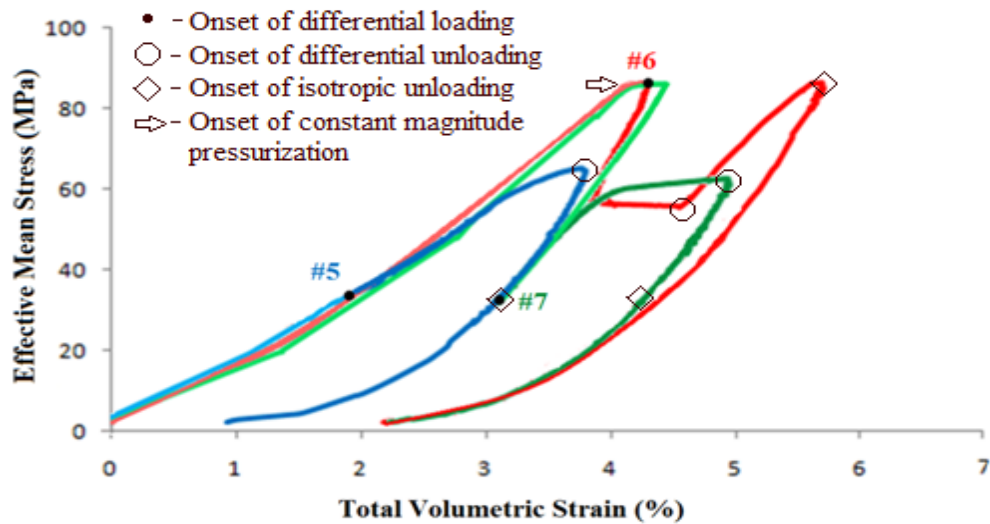
**Figure 14.** Effective mean stress, P, versus total (elastic & plastic) volumetric strain for samples loaded beyond failure in the transitional regime. Load paths shown are increasing mean stress (#5, blue curve), increasing mean stress after preconsolidation (#7, green curve), and decreasing mean stress (#6, red curve).

As expected for porous granular aggregates under isostatic stressing, the P versus total volumetric strain curves display concave upward shapes for both loading and unloading paths (Figure 14). The observed strain is dominantly, though not completely, poroelastic during these stages of the tests. Under differential loading the curves display concave downward shapes in plots of Q versus total axial strain, consistent with an increase in plastic strain except for concave upward shaped of curves in the early stages of differential loading (increasing Q; Figure 15).

The total volume strain and total axial strain at the onset of differential loading differ for the three load paths, and the change in the $\varepsilon$ for the differential loading through yield also varies from approximately 0.9% to 2.4% , which contrasts with the behavior seen in the ductile regime experiments (Table 4). Likewise, the $\beta$'s during differential

loading through yield vary dramatically, from 1.9% for the increasing P, and -0.35% for

the decreasing P load paths (Table 5). The partitioning between $\beta_e$ and $\beta_p$ is different for

the three load paths. Additional detail in the accumulation and partitioning of $\beta_e$ and $\beta_p$

can be obtained from the plots of P and Q versus plastic volume strain (Figures 16 and

17).



**Figure 15.** Differential stress, Q, versus total axial strain for samples loaded beyond failure in the transitional regime. Load paths shown are increasing mean stress (#5, blue curve), increasing mean stress after preconsolidation (#7, green curve), and decreasing mean stress (#6, red curve).
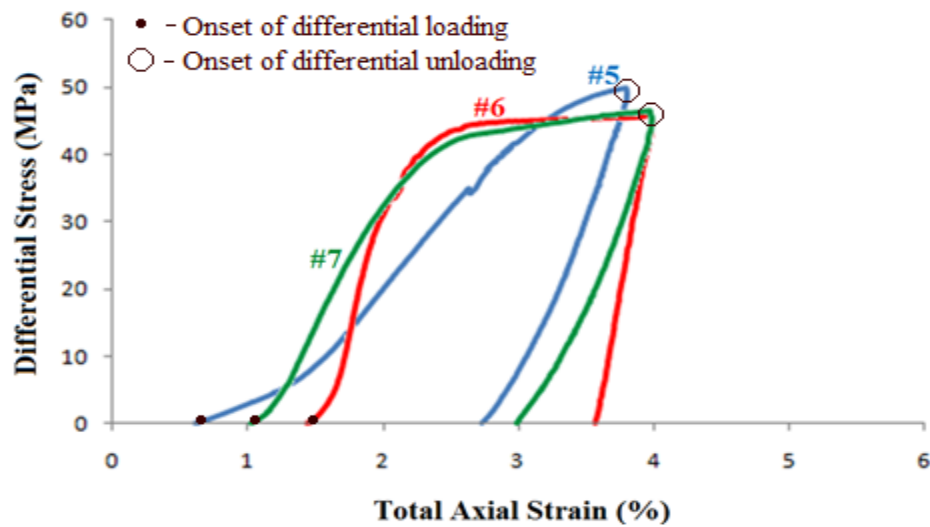
**Figure 16.** Effective mean stress, P, plastic volumetric strain for samples loaded beyond failure in the transitional regime. Load paths shown are increasing mean stress (#5, blue curve), increasing mean stress after preconsolidation (#7, green curve), and decreasing mean stress (#6, red curve).
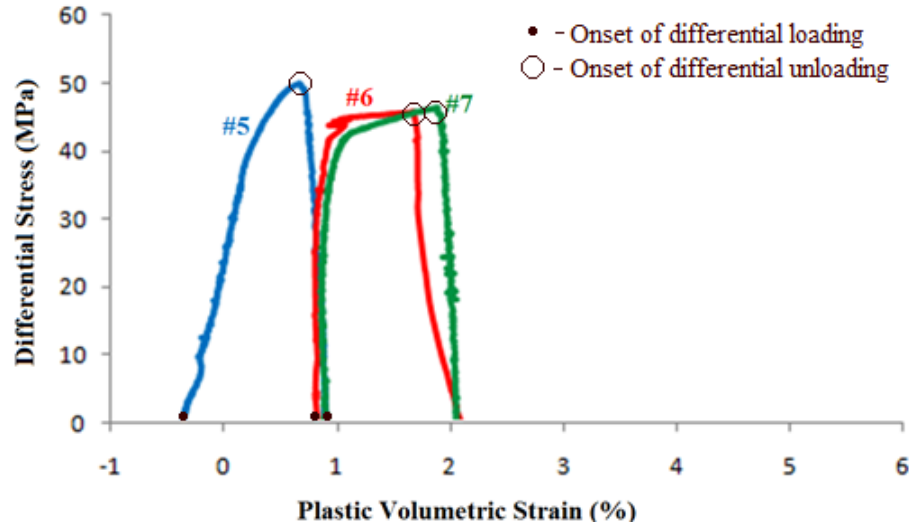


**Figure 17.** Differential stress, Q, plastic volumetric strain for samples loaded beyond failure in the transitional regime. Load paths shown are increasing mean stress (#5, blue curve), increasing mean stress after preconsolidation (#7, green curve), and decreasing mean stress (#6, red curve).
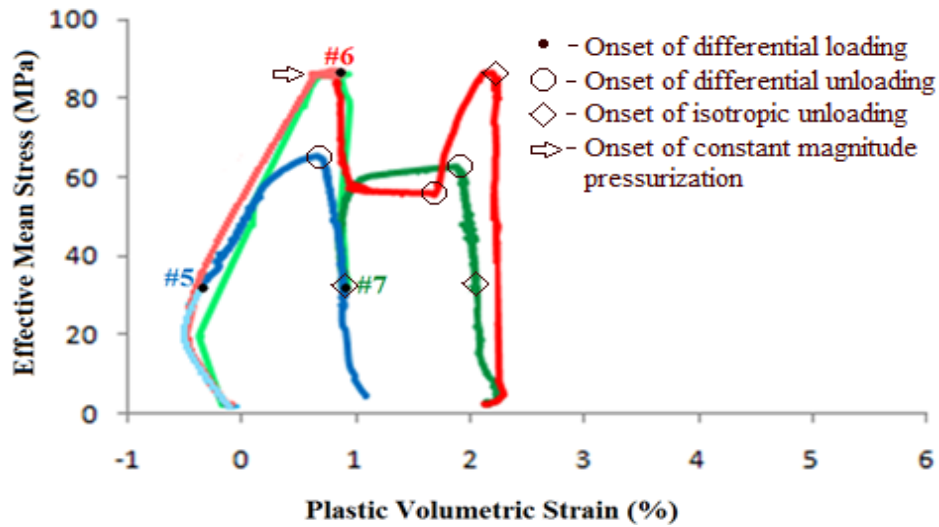
**Table 5.** Strain differences from the beginning of differential loads to the failure stress (C*) for the samples deformed in the transitional regime.

| Triaxial Compression Load Path | $\Delta\beta$ (%) | $\Delta\beta_p$ (%) | $\Delta\beta_e$ (%) | $\Delta\varepsilon$ (%) |
|---|---|---|---|---|
| Increasing P (#5) | +1.9 | +0.25 | +1.65 | +2.38 |
| Increasing P after Preconsolidation (#7) | +1 | +0.1 | +0.9 | +1.47 |
| Decreasing P (#6) | -0.35 | +0.03 | -0.38 | +0.88 |

In the transitional regime, significant $\beta_p$ accumulates during creep under high-magnitude isostatic stress in the preconsolidation portion of the increasing P test (#7) and before initiating differential loading in the decreasing P (#6) tests (Figure 16). However, the $\beta_p$ of the sample deformed under increasing P (#5), without preconsolidation is not significant prior to differential loading. During differential loading, significant $\beta_p$ begins to accumulate at a Q of approximately 40 MPa (Figure 17). The accumulation of $\beta_p$ during increasing Q prior to the failure is significant for only the sample deformed under increasing P with no preconsolidation (#5). For the load paths with a high magnitude initial pressurization (#6) and with a high magnitude preconsolidation (#7), $\beta_p$ significantly accumulates after the failure (Figures 16 and 17). To a lesser degree than that seen in the ductile regime, the sample deformed under decreasing P exhibits a significant $\beta_p$ during decreasing Q (Figures 16 and 17) reflecting a smaller dependence of compactional strain on both P and Q in the transitional regime. Samples deformed in the transitional regime exhibit little strain hardening after failure except for the increasing P load path without preconsolidation (#5). The greatest

apparent stiffness during the differential loading stage, relative to the other two samples, is seen in the decreasing P (#6) load path (Figure 15).

All samples deformed in the transitional regime exhibit lower apparent stiffness than those deformed in ductile regime in analogous load paths. Also, the post-failure hardening is greater for the samples deformed in the ductile regime than the samples deformed in the transitional regime as generally expected.In both the transitional and ductile regimes, samples deformed with increasing P and no preconsolidation (#5) show the greatest amount of volumetric strain during increasing Q prior to the failure (Table 4, 5). Samples deformed with increasing P after preconsolidation show medium apparent stiffness, compared with the other two samples deformed beyond failure in the transitional regime, likely due to the denser packing configuration achieved during preconsolidation.

4. DISCUSSION

## 4.1.  **Subcritical Deformation Mechanisms and Fabric Development**

The failure envelope for loose granular sand, as defined by *Karner et al.* [2005a] and employed herein, identifies the critical stress conditions for macroscopic failure. In this case macroscopic failure is defined by a significant increase in the rate of plastic deformation with progressive increase in mean or deviatoric stress, whether it be in the dilatant, low P regime, or in the compactional, high P regime.  Such failure may be identified by a number of criteria, e.g., axial and volume plastic strain and rate of acoustic emissions, but in terms of micromechanism, it is distinguished by onset of pervasive distributed or localized grain fracture, crushing and rearrangement.  As found in previous work [*e.g., Chester et al.,* 2004; *Karner et al.,* 2005a] and demonstrated by the present experiments, yielding occurs at stress levels below that for macroscopic failure at the critical stress, (i.e., during progressive loading plastic strain accumulates at subcritical stress states), for both isostatic and differential stress conditions.

The subcritical yielding in loose, granular, aggregates occurs by several different mechanisms during progressive increase in P and Q. Initially, at low stress levels, some compaction and shortening occurs by rigid body translation, rolling, and frictional sliding between intact grains [*Borg et al.,* 1960; *Lee and Farhoomand,* 1967, p.85]. As the grains achieve a more efficient, dense packing arrangement, the grain movements diminish and the aggregate may achieve a metastable equilibrium configuration [*Gallagher et al.,* 1974]. However, with continued loading, grain-to-grain contact stress

magnitudes increase and, for the most critically loaded contacts, become sufficient to induce intragranular fracture with associated separation and movement of particle fragments [*Karner et al.,* 2003]. Intragranular fracture can occur in an unstable fashion, or grow slowly through subcritical, chemically assisted crack propagation [*e.g., Chester et al.*, 2004]. During constant, unchanging subcritical isostatic or differential stress conditions, as in a creep test, plastic strains accumulate with time through subcritical fracture processes. This is demonstrated in the present work by the accumulation of strain during the preconsolidation portion of some of the load paths where plastic strain increases while P is constant (e.g., Figures 12 and 16).

The orientations of the grain scale microfractures are related to the orientation and relative magnitudes of the applied macroscopic stresses [*Gallagher et. al.,* 1974]. At various mean stress levels, when differential stress is large, intragranular cracks preferentially form parallel to maximum compressive stress axis [*e.g., Menendez et al.,* 1996].  In contrast, at elevated mean stress with low differential stress, intragranular fracture orientations are expected to display less preferred orientation, and fracture fabrics are likely random under isostatic loading.  Although samples deformed only by isostatic loading were not produced in this study, fracture orientations were determined in samples from previous consolidation experiments on sand aggregates. *Chester et al.* [2004] describe deformation of the same type of sand (St Peter Sand) aggregates subjected to creep compaction at effective pressures (Pe) of 34.5 and 70 MPa at temperatures of 22 °C. The durations of the creep tests were of the order of $2 \times 10^3$ s and plastic strain and fracturing occurred during creep.  These experiments are quite

analogous to the isostatic loading portions of the present experiments, and thus can provide information on the fracture fabric in samples prior to differential loading. Measurements of fracture orientation from photomicrographs of deformed samples of the study of *Chester et al.* [2004], are consistent with relatively random fabrics as expected for isotropic stressing (Figure 18).

The progressive change in fracture fabric documented here, from relatively random orientations at early stages of isostatic loading to strongly preferred orientations after macroscopic failure (Figure 18) is consistent with models in which fracture fabric strongly correlates with the macroscopic stress conditions at the time of fracture formation. Thus, fracture fabrics produced in the transitional regime from increasing P load path through failure and those produced during the preconsolidation stage of other load paths (prior to differential loading) will be much different (Figure 16) even though fracture densities are similar (e.g., samples 5 and 8 versus sample 9, Table 3) for these two loading conditions.
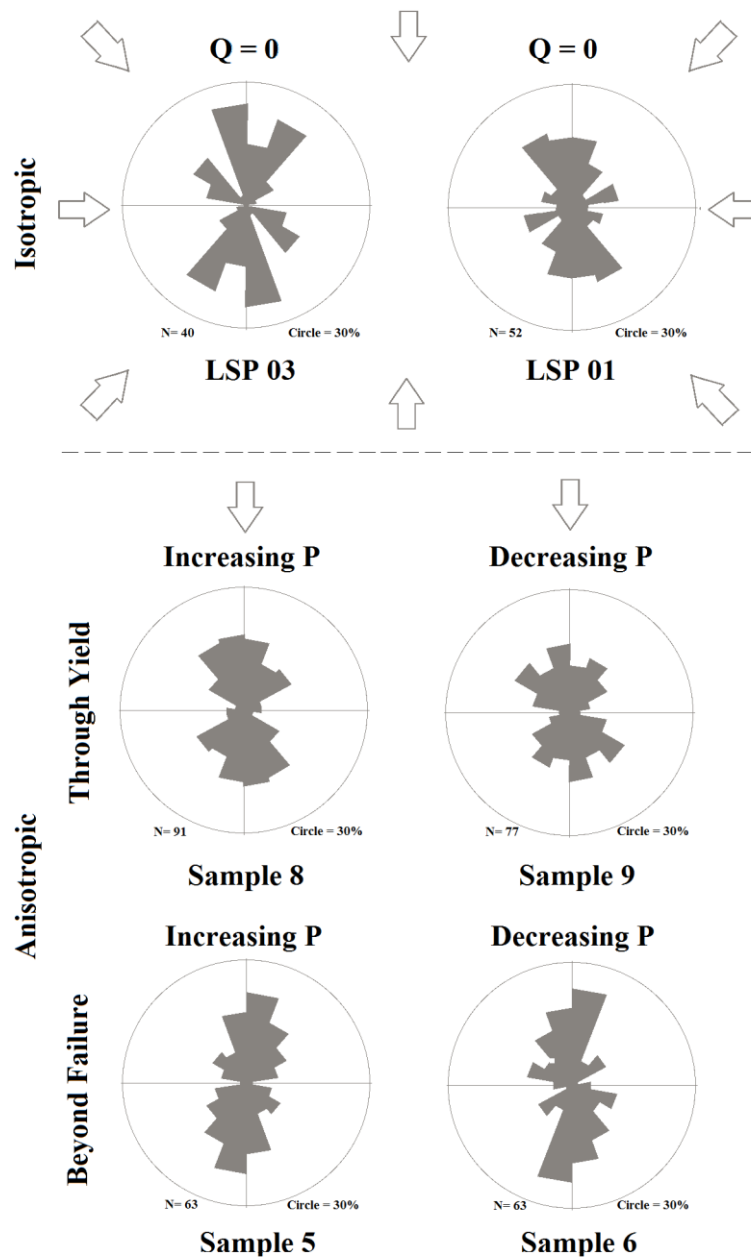
**Figure 18.** Evolution of preferred orientation of microfractures in samples deformed under isotropic load, deformed through yield, and deformed beyond failure in the transitional regime for different load paths and magnitudes of deformation. LSP03 and LSP01 samples are from the study by *Chester et al* [2005]. Orientations determined from petrographic sections cut through center of the specimen and perpendicular to the maximum principal compressive axis (see text). Outer perimeters of the rose diagram are the same frequency, 30%, in all diagrams. The number of measurements is indicated for each.

The steps taken to produce the sand aggregates, including the ultrasonic vibration, produced samples with average starting porosities within about 5% of the average porosity of all samples (about 34%, Table 2). However, it is likely that the local porosity varies much more within the samples where packing arrangements could vary between cubic type with porosity up to 47% and rhombohedral type packing with porosity down to 26%. We consider that the distribution of the initial packing configuration types throughout the samples is a critical factor for the magnitude of grain-to-grain contact stresses and thus the location of local porosity collapse and volume strain concentration. In the sand aggregate tests, the high porosity regions should consolidate first. Thus the plastic volume strain achieved during isostatic loading (e.g., the precompaction stage) will lead to more homogeneous porosity and packing distributions overall and thus will tend to reduce the initial heterogeneity of samples. At the beginning of the differential loading stage of each load path tested, the sample subjected to the increasing P load path should have the greatest variation in local packing configuration and porosity during differential loading. This could help explain the variation in the degree of localized deformation observed in the two samples subjected to the increasing P load path, and the fact that the sample loaded through yield has a greater degree of localization than the sample deformed past macroscopic failure (Figure 7).

## 4.2.   Load Path Effects

The stress state at failure of a porous granular material has a profound effect on the macroscopic mode of failure.  At high mean stress in the ductile compactional deformation regime, failure mode is generally distributed, whereas at low mean stress in the dilational regime, deformation is generally localized in the form of deformation bands [*e.g., Wong et al.,* 1997].  However, there is some debate concerning the effect of load path at subcritical stresses on macroscopic failure.

*Issen and Challa* [2003, 2008] analyze the effect of the intermediate principal stress, $\sigma_2$, on strain localization and mode of deformation in the transitional regime, using a bifurcation approach [*Rudnicki and Rice,* 1975], to predict band formation for two different constitutive models. They conclude that the orientation and type (compactional or dilational) of deformation bands vary significantly with change in $\sigma_2$. Cases of $\sigma_2$ close in magnitude to the maximum principal compressive stress favors dilational bands, and the cases of $\sigma_2$ close in magnitude to the minimum principal compressive stress favor compactional bands. Thus, for triaxial deformation experiments, triaxial compression is expected to favor compactional bands and triaxial extension is expected to favor dilational bands, provided the load path intersects the failure envelope in an appropriate failure regime.  This would suggest that load path may be particularly important to mode of failure in the transitional regime where both localization and compactional deformation is possible. Experimental support for these conclusions is provided by standard triaxial compression and extension experiments that

intersect the failure envelope at the same stress conditions, *e.g., Besuelle et al.* [2000, 2003]. However, direct testing of load path effects are relatively rare.

Load paths in Q-P stress space may be denoted by the ratio of change in Q to change in P, $\alpha = \Delta Q / \Delta P$. For standard triaxial testing, in which Pc is held constant during differential loading, the standard triaxial (axisymmetric) compression, ASC, load path is defined as $\alpha_{ASC} = 3$; where the increasing axial stress, $\sigma_1$, is more compressive than the constant confining pressure, $P_c = \sigma_2 = \sigma_3$. The standard axisymmetric extension, ASE, load path is defined by $\alpha_{ASE} = -3$; where the decreasing axial stress, $\sigma_3$, is always less compressive than the constant confining pressure, $P_c = \sigma_1 = \sigma_2$. A variety of nonstandard triaxial load paths are possible by changing Pc during compression or extension, as done by *Zhu et al.* [1997].

*Zhu et al.* [1997] employed a nontraditional axisymmetric extension load path where $\alpha_{Non-ASE} = 1.5$ and the confining pressure, $P_c = \sigma_1 = \sigma_2$, was increased while the axial stress, $\sigma_3$, was held constant. The triaxial load path with increasing P employed in the present study also has $\alpha$ equal to 1.5, but in this case the experiments are conducted in triaxial compression, (i.e. $P_c = \sigma_2 = \sigma_3$), and the Pc is synchronously increased at 4 times that of the increase in the axial stress, (i.e. $d\sigma_1 = 4\sigma_3$). Thus the ratio of $\alpha = \Delta Q / \Delta P$ for the ASE tests of *Zhu et al.* [1997] and the ASC increasing P tests are not the same because $\sigma_2$ differs.

*Zhu et al.* [1997] employed both standard triaxial compression load paths and the non-standard ASE load path described above to investigate possible load path effects on

the deformation, permeability, and failure mode of quartz-rich sandstones in the ductile, compactional regime. They conclude that the critical stress values for failure in the non-standard ASE and standard ASC tests are consistent, suggesting that critical compactional strength, C*, is not sensitive to load path. The experiments on the sand aggregates, reported here represent a similar deformation regime as the experiments of *Zhu et al.* [1997]. The results for critical strength for failure of sand aggregates are approximately the same for the three different load paths.  In particular, the differential stress versus plastic volumetric strain plots for the load paths of increasing P with preconsolidation and decreasing P are very similar (Figure 14). However, results of tests at increasing P (without preconsolidation, #5) are slightly different from those of the other two tests, displaying a lower yield stress, somewhat more plastic yielding prior to macroscopic failure, and slightly lower failure strength (Figure 13).

The experiments on the sand aggregates in the transitional regime indicate that the failure strength is fairly similar for each load path.  The failure strength indicated in the P and Q versus plastic volumetric strain plots is essentially the same for the load paths of increasing P with preconsolidation and decreasing P.  In addition, post failure strengths are similar for both these load paths.  Results of the test with increasing P (without preconsolidation) exhibit similar failure strength, but stress-strain data show greater work hardening and ultimately greater post-failure strength, compared with results of the other two load paths.  For both the ductile and transitional regimes, the mechanical response of sand aggregates at increasing P (without a preconsolidation

stage) is most dissimilar from the others. The behavior of samples subjected to increasing P (with preconsolidation) and decreasing P are generally the same.

The microstructural evolution and production of localized zones of compaction in the transitional regime appear to be similar for load paths of increasing P (with preconsolidation) and decreasing P.  Microstructures of the samples that experienced increasing P without preconsolidation stage are different from microfractures of the other samples.  Thus, on the basis of both mechanical response and microstructure, it appears that load path has relatively small effect on deformation response.  However, the initial stage of consolidation at relatively high isostatic stress at subcritical stresses may have a significant effect of deformation response.

*Karner et.al,* [2005] showed porosity evolution contours plot in the Q-P space using the results of standard ASC tests on the same sand employed herein. The contours generally are aligned parallel to differential stress, Q, axis, i.e., demonstrate a strong P dependence. A similarly constructed contour plots based on the mechanical data of the increasing P-ASC load path employed within present study is quite similar to those presented by *Karner et.al,* [2005], whereas the contours pattern based on the mechanical data of the decreasing P-ASC load path tests employed within present study show a different P and Q dependence (Figures 19, 20 and 21).
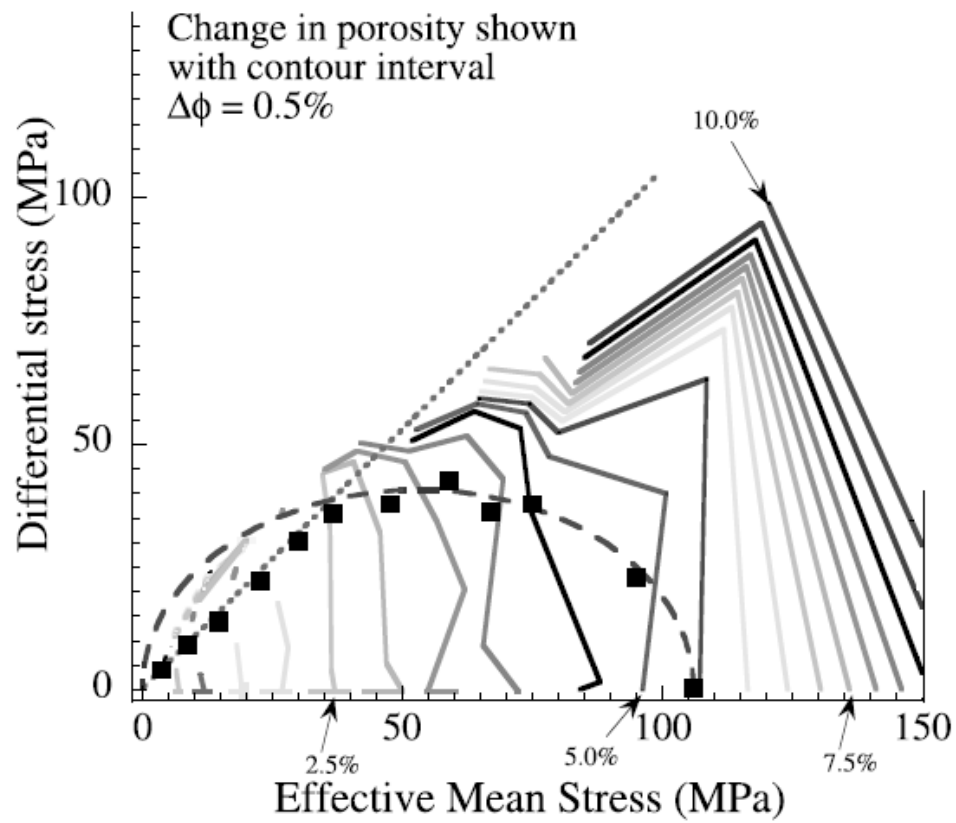
**Figure 19.** Porosity evolution contours plotted depending on mechanical results of the standard ASC tests on St. Peter Sand samples employed by *Karner et.al.* [2005].
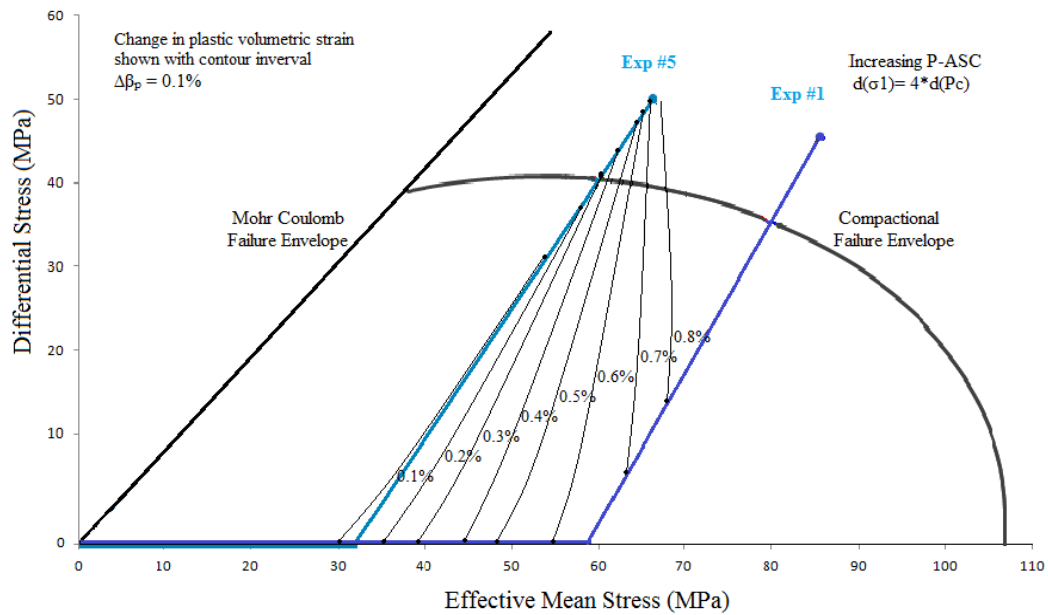
**Figure 20**. Porosity evolution contours plotted in the Q-P space depending on mechanical results of increasing P-ASC load path tests employed in the present study.
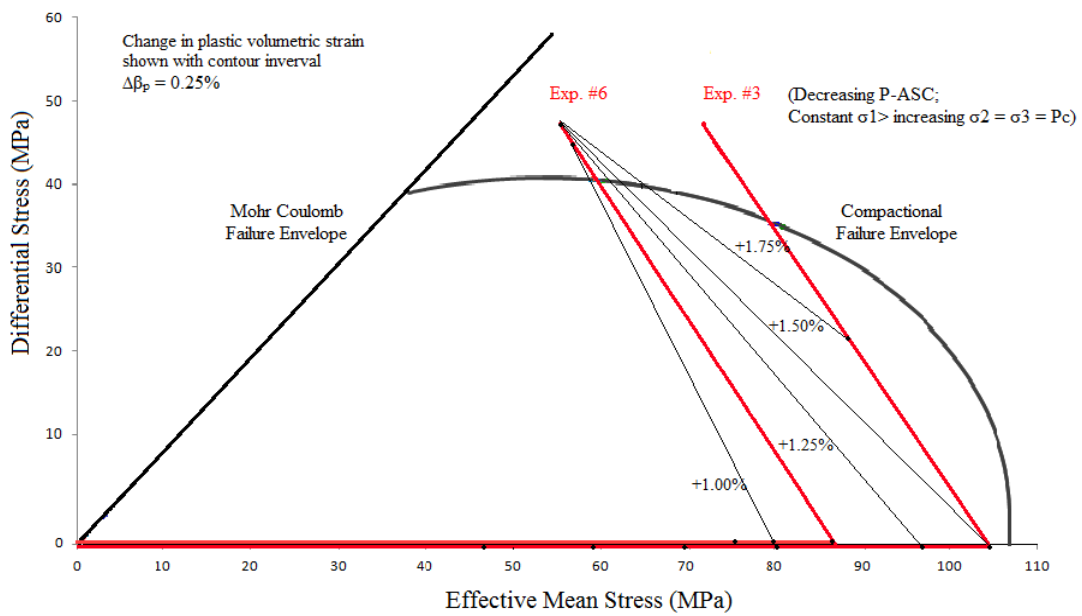


**Figure 21.** Porosity evolution contours plotted in the Q-P space depending on mechanical results of decreasing P-ASC load path tests employed in the present study.

### 4.3.    Comparison with Natural Examples of Compaction Bands

Lenticular and thin (a few grain thick) geometric features of the localized compactional deformation bands produced in the present study may be likened to the crooked compaction bands encountered in nature as described by *Mollema and Antonellini* [1996]. However, the small sample size and the incohesive nature of our samples compared with natural buried sediments could influence the localization and extent of the compactional deformation bands within experiements. Also, estimating possible extent of the band plane-parallel elongation of the compaction bands in our samples is difficult due to the limited scale of our samples.

5.  SUMMARY AND CONCLUSIONS

Macroscopic failure of well-sorted, porous, quartz sand aggregates under non-standard triaxial compression load paths occurs at stress states consistent with the critical stress envelope for failure determined through standard triaxial compression loading. These results indicate that, to first order, critical stress for macroscopic failure has little dependence on load path.

In contrast to the load path effects, preconsolidation of the sand aggregates by isotropic loading at levels below the critical stress for macroscopic failure has a significant effect on mechanical behavior and character of deformation at failure.  For similar differential load paths, preconsolidation at subcritical isotopic stress favors less yielding prior to failure and less hardening post failure for both the transitional and ductile deformation regimes.

In the transitional deformation regime, preconsolidation favors the formation of localized compactional deformation zones oriented perpendicular to the maximum principal compression direction by fracture, grain crushing and porosity collapse.

Microfracture fabrics generally reflect the stress conditions at the time of plastic strain where isotopic stress favors random fabrics and differential stress favors anisotropic fabrics with a preferred orientation of microfractures parallel to the maximum compressive stress direction.  Microfracture orientation within compactional deformation bands display strong preferred orientation parallel to the maximum principal compression direction.

REFERENCES

Besuelle, P., J. Desrues, and S. Raynaud, (2000), Experimental characterisation of the localization phenomenon inside a Vosges sandstone in a triaxial cell. *International Journal of Rock Mechanics and Mining Sciences, 37*, 1223-1237.

Bésuelle P., P. Baud, and Wong T. (2003), Failure mode and spatial distribution of damage in Rothbach sandstone in the brittle-ductile transition, *Pageoph 160* No 5-6, pp. 851-868

Borg. I.. M. Friedman, J. Handin, and D. V. Higgs (1960), Experimental deformation of St. Peter Sand: A study of cataclastic flow, in Rock Deformation, edited by D. Griggs and J. Handin, *Geol. Soc. Am., Mem*., 79, 133. pp. 133 191. *Geological Society of America*. New York.

Chester, F.M., (1988), The transition from cataclasis to intracrystalline plasticity in experimental shear zones, Ph.D. thesis, Texas A&M University, College Station, pp. 67-69.

Chester, J. S., S. C. Lenz, F. M. Chester, and R. A. Lang (2004), Mechanisms of compaction of quartz sand at diagenetic conditions, *Earth Planet. Sci. Lett.*, *220*(3-4), 435– 451.

Choens, R. C. and F. M. Chester (2009), Characterizing Damage Evolution and Yield in Sandstone Under Triaxial Loading as a Function of Various Effective Pressure. *AGU Annual Convention and Exhibition Denver*, June 7-10

Gallagher, J.J., M. Friedman, J. Handin, and G. Sowers, (1974), Experimental studies relating to microfracture in sandstone. *Techtonophysics*, *21*: 203-247.

He, W. W. (2001), Experimental and theoretical modeling of creep compaction of quartz sand: Rate laws and evolution of porosity and fluid chemistry, Ph.D. thesis, 140 pp., Texas A&M Univ., College Station, TX.

Heard, H. C. (1963), Effect of large changes in strain rate in the experimental deformation of Yule Marble. *J. Geol., 71*, 162–195.

Holcomb D, J.W. Rudnicki, K.A. Issen and K. Sternlof, (2007), Compaction localization in the earth and the laboratory: State of the research and research directions. *Acta Geotechnica*; *2*:1–15.

Issen, K.A. and V. Challa, (2003), Conditions for dilation band formation in granular materials. *Proceedings of the ASCE Engineering Mechanics Conference* 16th, pp. 1 – 4, University of Washington, Seattle.

Issen, K. A., and V. Challa (2008), Influence of the intermediate principal stress on the strain localization mode in porous sandstone, *J. Geophys. Res., 113*, B02103, doi: 10.1029/2005JB004008.

Jeng, F.-S., M.-C. Weng, T.-H. Hunag and M.-L. Lin, (2002), Deformational characteristics of weak sandtone and impact to tunnel deformation. *Tunnel. Undergr Space Tech. 17*:263-274.

Karner, S. L., F. M. Chester, A. K. Kronenberg, and J. S. Chester (2003), Subcritical compaction and yielding of granular quartz sand. *Tectonophysics*, *377*, 357– 381.

Karner, S. L., J. S. Chester, F. M. Chester, A. K. Kronenberg, and A. Hajash Jr. (2005), Laboratory deformation of granular quartz sand: Implications for the burial of clastic rocks. *AAPG Bull.*, *89*, 603– 625.

Lee, K. L., and I. Farhoomand (1967), Compressibility and crushing of granular soil in anisotropic triaxial compression, *Can. Geotech*. J., *4*: 68-99.

Lenz, S. C. (2002), Acoustic emission and compaction creep of quartz sand at subcritical stress, M.S. thesis, p. 62. Texas A&M University, College Station.

Mollema, P.N., and M.A. Antonellini, (1996), Compaction bands: A structural analog for anti-mode I cracks in aeolian sandstone. *Tectonophysics 267*: 209-228,

Olsson, W. A., (1999), Theoretical and experimental investigation of compaction bands in porous rock. *J. Geophys. Res., 104*, 7219-7228.

Olsson, W.A., and D.J. Holcomb, (2000), Compaction localization in porous rock. *Geophys. Res. Lett. 27*: 3537-3540.

Olsson, W.A., D.J. Holcomb, and J.W. Rudnicki, (2002), Compaction localization in porous sandstone: Implications for reservoir mechanics. *Oil Gas Sci. Technol. 57* (5), 591–599.

Rudnicki J.W. and J.R. Rice, (1975), Conditions for the localization of deformation in pressure-sensitive dilatant materials. *J. Mech. Phys. Solids*, *23*, 371-394.

Wong, T.-f., C. David, and W. Zhu, (1997), The transition from brittle faulting to cataclastic flow in porous sandstones: Mechanical deformation. *Geophys. Res. 102*: 3009-3025.

Zhu W, L.G.J. Montesi and T-f. Wong, (1997), Shear-enhanced compaction and permeability reduction: Triaxial extension tests on porous sandstone. *Mech Mater*; *25*:199-214.

VITA

**Gokturk Mehmet Dilci**

Dept. of Geology & Geophysics, Texas A&M University, MS 3115,

College Station, TX 77843

gokturkmehmet08@geo.tamu.edu

**Education**

M.S., Geology, Texas A&M University, College Station, TX, May 2010

B.S., Geology, University of Ankara, Ankara, Turkiye, June 2006

**Fellowships & Awards**

- Republic of Turkey, Ministry of National Education and Turkish Petroleum Corporation - Fellowship and Graduate Assistantship for M.A Study in the United States (2007-2011)
- Republic of Turkey, Ministry of National Education and Turkish Petroleum Corporation - Fellowship and Stipend for the Study of English and any other foreign language(s) (2007-2011)
- The World Bank, in the "Turkey Creative Development Ideas" project competition, went on the Semifinal with the project of "Nature Education Center" (2004)

**Internships**

- *Turkish Petroleum Corporation*                    Ankara, Turkiye
                                                                          June 2004 - September2004

- *TEKMAR Mining Exploration Company*            Mersin, Turkiye
                                                                          June 2005 – July 2005

- *COPUROGLU Marble & Granite Engineering,*      Mersin, Turkiye
  *Industry, and Commercial Company /*          August 2005 –September
  2005
  *Land Reserve Endeavour / Trainee*